

COMPUTATION OF RADAR CROSS SECTIONS OF COMPLEX TARGETS  
BY SHOOTING AND BOUNCING RAY METHOD

A THESIS SUBMITTED TO  
THE GRADUATE SCHOOL OF NATURAL AND APPLIED SCIENCES  
OF  
MIDDLE EAST TECHNICAL UNIVERSITY

BY

SALİM ÖZGÜN

IN PARTIAL FULFILLMENT OF THE REQUIREMENTS  
FOR  
THE DEGREE OF MASTER OF SCIENCE  
IN  
ELECTRICAL AND ELECTRONICS ENGINEERING

AUGUST 2009

Approval of the thesis:

**COMPUTATION OF RADAR CROSS SECTIONS OF COMPLEX  
TARGETS BY SHOOTING AND BOUNCING RAY METHOD**

Submitted by **SALİM ÖZGÜN** in partial fulfillment of the requirements for the degree of **Master of Science in Electrical and Electronics Engineering, Middle East Technical University** by,

Prof. Dr. Canan Özgen  
Dean, Graduate School of **Natural and Applied Sciences** \_\_\_\_\_

Prof. Dr. İsmet Erkmen  
Head of Department, **Electrical and Electronics Engineering** \_\_\_\_\_

Prof. Dr. Mustafa Kuzuoğlu  
Supervisor, **Electrical and Electronics Engineering, METU** \_\_\_\_\_

**Examining Committee Members:**

Prof. Dr. Gönül Turhan Sayan  
Electrical and Electronics Engineering, METU \_\_\_\_\_

Prof. Dr. Mustafa Kuzuoğlu  
Electrical and Electronics Engineering, METU \_\_\_\_\_

Prof. Dr. Gülbin Dural  
Electrical and Electronics Engineering, METU \_\_\_\_\_

Assist. Prof. Dr. Lale Alatan  
Electrical and Electronics Engineering, METU \_\_\_\_\_

Assist. Prof. Dr. Egemen Yılmaz  
Electronics Engineering, Ankara University \_\_\_\_\_

**Date:**

**I hereby declare that all information in this document has been obtained and presented in accordance with academic rules and ethical conduct. I also declare that, as required by these rules and conduct, I have fully cited and referenced all material and results that are not original to this work.**

Name, Last name: Salim Özgün

Signature :

## **ABSTRACT**

### **COMPUTATION OF RADAR CROSS SECTIONS OF COMPLEX TARGETS BY SHOOTING AND BOUNCING RAY METHOD**

Özgün, Salim

M.Sc., Department of Electrical and Electronics Engineering

Supervisor: Prof. Dr. Mustafa Kuzuoğlu

August 2009, 66 Pages

In this study, a MATLAB® code based on the Shooting and Bouncing Ray (SBR) algorithm is developed to compute the Radar Cross Section (RCS) of complex targets. SBR is based on ray tracing and combine Geometric Optics (GO) and Physical Optics (PO) approaches to compute the RCS of arbitrary scatterers. The presented algorithm is examined in two parts; the first part addresses a new aperture selection strategy named as “conformal aperture”, which is proposed and formulated to increase the performance of the code outside the specular regions, and the second part is devoted to testing the multiple scattering and shadowing performance of the code. The conformal aperture approach consists of a configuration that gathers all rays bouncing back from the target, and calculates their contribution to RCS. Multiple scattering capability of the algorithm is verified and tested over simple shapes. Ray tracing part of the code is also used as

a shadowing algorithm. In the first instance, simple shapes like sphere, plate, cylinder and polyhedron are used to model simple targets. With primitive shapes, complex targets can be modeled up to some degree. Later, patch representation is used to model complex targets accurately. In order to test the whole code over complex targets, a Computer Aided Design (CAD) format known as Stereo Lithography (STL) mesh is used. Targets that are composed in CAD tools are imported in STL mesh format and handled in the code. Different sweep geometries are defined to compute the RCS of targets with respect to aspect angles. Complex targets are selected according to their RCS characteristics to test the code further. In addition to these, results are compared with PO, Method of Moments (MoM) and Multilevel Fast Multipole Method (MLFMM) results obtained from the FEKO software. These comparisons enabled us to improve the code as possible as it is.

Keywords: Shooting and Bouncing Ray (SBR) Method, Radar Cross Section (RCS), Conformal Aperture, FEKO

# ÖZ

## KARMAŞIK HEDEFLERİN RADAR KESİT ALANININ SEKEN IŞIN YÖNTEMİYLE HESAPLANMASI

Özgün, Salim

Yüksek Lisans, Elektrik-Elektronik Mühendisliği Bölümü

Tez Yöneticisi: Prof. Dr. Mustafa Kuzuoğlu

Ağustos 2009, 66 sayfa

Bu çalışmada cisimlerin Radar Kesit Alanının (RKA) hesaplanması için Seken Işın Yöntemi (SIY) algoritması kullanılarak MATLAB® tabanlı bir kod geliştirilmiştir. SIY rastgele seçilmiş hedeflerin RKA değerini hesaplamak için Geometrik Optik (GO) ve Fiziksel Optik (FO) yöntemlerini beraber kullanan ışın takibine dayalı bir algoritmadır. Sunulan algoritma iki bölümde incelenmiştir; ilk bölümde doğrudan yansıma dışında kalan bölgelerde kodun performansını artırmak için yeni bir yöntem olan “uyumlu açıklık” önerilmiş ve formüle edilmiş, ikinci bölümde ise algoritmanın çoklu yansımaları hesaplama ve gölgeleme performansı test edilmiştir. ”Uyumlu açıklık” yöntemi ile hedeften geri seken

tüm ışınlar toplanıp RKA' ya katkıları hesaplanmıştır. Algoritmanın çoklu yansıma kabiliyeti sadece basit şekiller üzerinde test edilmiştir. Kodun ışın takibi bölümü aynı zamanda gölgeleme algoritması olarak kullanılmıştır. İlk aşamada basit hedefleri modellemek için küre, plaka, silindir ve polihedron gibi basit şekiller kullanılmıştır. Ancak basit şekiller ile karmaşık hedefler bir dereceye kadar modellenebilmektedir. Daha sonraki aşamalarda karmaşık şekillerin daha iyi modellenebilmesi için üçgen parçalar kullanılmıştır. Kodu karmaşık hedefler üzerinde test etmek için Bilgisayar Destekli Tasarım (BDT) formatı olan STL ağ yapısı kullanılmıştır. BDT ortamında modellenen hedefler STL ağ formatında koda taşınmış ve işlem yapılmıştır. Cisimlerin RKA değerlerini bakış açısına göre hesaplayabilmek için farklı döndürme geometrileri kullanılmıştır. Seçilen karmaşık hedeflerde RKA karakteristiklerinin farklı olması göz önünde bulundurulmuştur. Bu çalışmalara ek olarak koddan elde edilen sonuçlar, FEKO yazılımından elde edilen FO, MoM ve MLFMM sonuçları ile karşılaştırılmıştır. Bu karşılaştırma, kodu mümkün olduğunca geliştirme imkânını bize sunmuştur.

Anahtar Sözcükler: Seken Işın Yöntemi (SIY), Radar Kesit Alanı (RKA), Uyumlu Açıklık, FEKO

*To my Family*

## ACKNOWLEDGEMENTS

I would like to thank my thesis supervisor, Prof. Dr. Mustafa Kuzuođlu for his guidance, understanding and suggestions. His broad vision and motivation has been a great privilege.

I would also thank my leader Harun Solmaz and age of empires team; Mehmet Karakaş, Selim Kocabay, Mehmetcan Apaydın, Seçkin Arıbal, Aykut Cihangir, Musa Civil, Erdem Kazaklı, Baran Kızıltan and Şükrü Bülent Toker for their great friendship and enjoyable “age of empires the conquerors” times during lunch.

Also, I would like to express my thanks to my family for their understanding and patience.

Lastly, thanks to TAI for supplying the FEKO software and supporting me for this work.

# TABLE OF CONTENTS

ABSTRACT.....	iv
ÖZ.....	vi
ACKNOWLEDGEMENTS.....	ix
TABLE OF CONTENTS.....	x
LIST OF TABLES.....	xii
LIST OF FIGURES.....	xiii
LIST OF FIGURES.....	xiii
CHAPTER	
1 INTRODUCTION.....	1
1.1 <i>Literature Review</i> .....	3
1.2 <i>Overview of the Thesis</i> .....	4
1.3 <i>Outline of the Thesis</i> .....	5
2 SHOOTING AND BOUNCING RAY METHOD.....	7
2.1 <i>Formulation of the Shooting and Bouncing Ray Method</i> .....	8
2.2 <i>Numerical Results for Simple Targets</i> .....	19
2.3 <i>SBR Final Integration Aperture</i> .....	39
2.4 <i>SBR Multiple Scattering Capability</i> .....	44
2.5 <i>Shadowing</i> .....	46
3 APPLICATION OF SBR TO COMPLEX TARGETS.....	48

3.1	<i>Target Modeling</i> .....	49
3.2	<i>Target Rotation</i> .....	52
3.3	<i>Numerical Results</i> .....	53
4	CONCLUSIONS .....	61
4.1	<i>Summary of the Thesis</i> .....	61
4.2	<i>Advantages and Disadvantages of SBR</i> .....	62
4.3	<i>Future Work</i> .....	63
	REFERENCES .....	65

## LIST OF TABLES

### TABLES

Table 3-1 Computation times for tank model simulation .....	54
Table 3-2 Computation times for ship model simulation .....	56
Table 3-3 Computation times for F-117 model simulation .....	58

# LIST OF FIGURES

## FIGURES

Figure 2.1 SBR, incident rays and exit aperture .....	9
Figure 2.2 Triangle defined with right hand rule.....	11
Figure 2.3 A triangle constructed from three half spaces .....	12
Figure 2.4 Reflection of a ray .....	13
Figure 2.5 Ray tube.....	16
Figure 2.6 Shape of exit ray tube.....	18
Figure 2.7 Simulation setup for monostatic RCS of PEC plate.....	21
Figure 2.8 Comparison of MoM and SBR results for $\theta\theta$ polarized monostatic RCS of PEC plate with respect to frequency .....	22
Figure 2.9 Simulation setup for bistatic RCS of PEC plate.....	23
Figure 2.10 Comparison of MoM and SBR results for $\theta\theta$ polarized bistatic RCS of PEC plate with respect to frequency .....	23
Figure 2.11 Simulation setup for monostatic RCS of PEC plate.....	24
Figure 2.12 Comparison of MoM and SBR results for $\theta\theta$ polarized monostatic RCS of PEC plate .....	25
Figure 2.13 Comparison of PO and SBR results for $\theta\theta$ polarized monostatic RCS of PEC plate.....	26
Figure 2.14 Simulation setup for bistatic RCS of PEC plate.....	27
Figure 2.15 Comparison of MoM and SBR results for $\theta\theta$ polarized bistatic RCS of PEC plate.....	28
Figure 2.16 Simulation setup for bistatic RCS of PEC plate.....	29
Figure 2.17 Comparison of MoM and SBR results for $\theta\theta$ polarized bistatic RCS of PEC plate with respect to frequency .....	30
Figure 2.18 Simulation setup for monostatic RCS of PEC flare-like shape.....	31

Figure 2.19 Comparison of PO and SBR results for $\theta\theta$ polarized monostatic RCS of PEC flare-like shape for planar aperture case .....	32
Figure 2.20 Comparison of PO and SBR results for $\theta\theta$ polarized monostatic RCS of PEC flare-like shape for conformal aperture case .....	33
Figure 2.21 Simulation setup for monostatic RCS of PEC arbitrary polyhedron.	34
Figure 2.22 Comparison of PO and SBR results for $\theta\theta$ polarized monostatic RCS of PEC arbitrary polyhedron.....	34
Figure 2.23 Comparison of PO and SBR results for $\theta\theta$ polarized monostatic RCS of PEC arbitrary polyhedron after correction on shadowing algorithm .....	35
Figure 2.24 Shadowing effect.....	36
Figure 2.25 Comparison of PO, MoM and SBR results for $\theta\theta$ polarized monostatic RCS of PEC arbitrary polyhedron.....	37
Figure 2.26 Simulation setup for monostatic RCS of PEC arbitrary shape.....	38
Figure 2.27 Comparison of PO and SBR results for $\theta\theta$ polarized monostatic RCS of PEC arbitrary shape.....	38
Figure 2.28 Planar exit aperture approach .....	40
Figure 2.29 Monostatic RCS of PEC cube with planar exit aperture approach ...	41
Figure 2.30 Conformal exit aperture approach.....	43
Figure 2.31 Monostatic RCS results with conformal exit aperture approach.....	44
Figure 2.32 Simulation setup for monostatic RCS of PEC dihedral .....	45
Figure 2.33 Comparison of PO, MoM and SBR results for $\theta\theta$ polarized monostatic RCS of PEC dihedral.....	46
Figure 2.34 Shadowing problem.....	47
Figure 3.1 Target and Ray Window Geometry.....	49
Figure 3.2 STL mesh structure .....	50
Figure 3.3 Simulation setup for monostatic RCS of PEC triangular patch .....	51
Figure 3.4 Comparison of MoM and SBR results for $\theta\theta$ polarized monostatic RCS of PEC triangle .....	51
Figure 3.5 Fixed rotation around Y axis .....	53
Figure 3.6 Tank model constructed from 132 triangular patches.....	54

Figure 3.7 Comparison of PO and SBR results for $\theta\theta$ polarized monostatic RCS of PEC tank model.....	55
Figure 3.8 Monostatic RCS of ship model .....	56
Figure 3.9 Comparison of PO, MLFMM and SBR results for $\theta\theta$ polarized monostatic RCS of PEC ship model .....	57
Figure 3.10 F-117 model .....	58
Figure 3.11 Comparison of PO and SBR results for $\theta\theta$ polarized monostatic RCS of PEC F-117 model .....	59
Figure 3.12 Comparison of MoM and SBR results for $\theta\theta$ polarized monostatic RCS of PEC F-117 model.....	59

# CHAPTER 1

## INTRODUCTION

During the second half of 19<sup>th</sup> century, James Clerk Maxwell completed the classical theory of electromagnetism, synthesizing all the previous knowledge developed by prominent physicists and mathematicians such as Coulomb, Ampere, Oersted, Faraday and Hertz. His famous equations, known as “Maxwell Equations”, have been widely used until the present time by physicists and engineers in numerous applications. A major application area of Maxwell’s equations is scattering of electromagnetic waves by obstacles. This topic gained a lot of importance after the development of radar systems during World War II. In radar applications, the electromagnetic power intercepted by a target is modeled via a hypothetical area known as Radar Cross Section (RCS). The power intercepted by the object is calculated as the product of RCS and the power density at the target location. As a result, calculation of the RCS of targets is one of the important aspects of radar engineering.

The RCS of an object is closely related of the constitutive parameters (permittivity, permeability and conductivity) and the geometry (or shape). In designing targets almost invisible to radars (i.e. stealth targets), it is the parameter that should be minimized. In early 1970s, stealth technology has become popular, with a lot of emphasis placed on reduction of the RCS of targets. Even though the modern view of stealth design is to achieve an optimum balance between RCS

reduction, incorporation of Electromagnetic Warfare (EW) and operational performance; RCS reduction is still the most important aspect of stealth technology. Modern radars are not only capable of detecting low RCS targets, but they can examine and classify targets according to their scattering characteristics. The main task of RCS design engineer is to introduce stealth targets effectively invisible to these powerful modern radars. At this point, developers of stealth targets use extensively the tools of Computational Electromagnetics (CEM) to simulate the scattering of electromagnetic waves by targets with complex geometry and/or electrical parameters.

The methods of CEM are based on the numerical approximation of Maxwell's Equations for modeling the interaction of electromagnetic fields with objects. During the last few decades this area has become crucial for stealth engineering. The same methods are also used extensively in antenna design and placement, radome design, electromagnetic compatibility (EMC) analysis, RF component design and bio-electromagnetics problems. Many computational electromagnetics methods have been developed and implemented to solve different kinds of problems. Basically, these methods can be classified into two groups, namely as full-wave and approximate solution techniques.

Full-wave methods have been developed for the numerical discretization and approximation of equations deduced from Maxwell's equations. The Method of Moments (MoM), Finite Difference Time Domain (FDTD) method and Finite Element Method (FEM) are the most commonly-used full-wave methods. These methods are sometimes named as low frequency methods because of the requirement of high computer resources at high frequencies. In recent years, some new full-wave based methods have been introduced in order to solve electrically large problems. For example, the Multilevel Fast Multi Pole Method (MLFMM) is a method that uses the formulation of MoM. Its main difference from the MoM is that it groups the basis functions and calculates the interaction between these groups. Through this modification, this approach can handle electrically large

problems such as dielectric structures with memory and run-time requirements formidable even for today's super computers.

Approximate solutions are implemented basically to handle electrically large problems. Since these methods are effective at high frequencies, they are also known as high frequency solution techniques. Basic high frequency techniques are Physical Optics (PO), Geometric Optics (GO), Physical Theory of Diffraction (PTD), Geometric Theory of Diffraction (GTD) and Uniform Theory of Diffraction (UTD). PO and GO can give good solutions in specular regions but for complex structures their results are not very reliable. Utilization of GTD and PTD can improve the results of PO and GO in regions where diffracted rays dominate. In stealth designs, since specular reflections are avoided, calculation of the RCS must take into consideration the effect of diffraction and multiple reflections. Contribution of diffraction can be calculated with PTD. In recent years a new method, namely the Shooting and Bouncing Ray (SBR) method is implemented to solve the effects of multiple scattering. SBR is a method that uses a combination of the GO and PO techniques. It is a ray tracing technique suitable to use in stealth design applications.

## ***1.1 Literature Review***

Multiple Scattering plays an important role in RCS calculation. Cavity structures (such as jet-engine inlets) are the regions where multiple scattering phenomenon occurs. Since such structures contribute extensively to RCS, the analysis of this problem has been an important topic in RCS literature. Traditionally, RCS of cavity structures were calculated by model analysis or full wave methods. For complex structures, model analysis was not adequate, and full wave methods were not capable of solving electrically large problems. In 1987, SBR was implemented for the first time by Chou *et al.* [1] in a project work supported by NASA. In this method, rays are launched towards the cavity and traced inside with GO rules. Material properties of the cavity walls are taken into account and

rays are captured in the cavity opening in order to calculate the far field values. Later, Ling *et al.* presented this work as an article in [2].

SBR has been developed originally for cavity structures, but Baldauf *et al.* modified this technique for open scatterers [3]. In cavity structures, rays that leave the cavity are captured in the cavity opening. However for open scatterers the final integration aperture is not easy to choose. In [3], an aperture that coincides with the scatterer itself is suggested. With this aperture choice, the solution is identical to the conventional PO solution, except that multiple scattering effects of the rays are also modeled. In this work, formulation is based on Huygens' Principle.

In 2005, to extend the capability of SBR for the simulation of scattering from diffusive and grating structures, Diffusive Ray Algorithm is introduced by Galloway *et al.* [4]. This algorithm reduces to the basic SBR formulation for targets constructed as a superposition of flat plates, but for curved structures a single ray tube that reflects from a curved part will generate a family of other ray tubes [4].

## ***1.2 Overview of the Thesis***

In this thesis, a basic SBR code is developed in MATLAB. Numerical results taken from the code are compared with the results obtained from FEKO software. FEKO is an electromagnetic (EM) analysis software which includes both full-wave and approximate solution methods and which has the capability to solve a wide range of electromagnetic problems [5]. For simple targets results are obtained from FEKO's MoM and PO solvers. For electrically large problems results are obtained from MLFMM solver in a redhat based super computer with 18GB RAM.

SBR code is tested over simple targets like plate, dihedral and cube for monostatic and bistatic RCS calculations, for a range of frequencies. To test the SBR code for target in which multiple scattering phenomena is effective, a dihedral was used. Clearly, scattering from targets like dihedral and trihedral is dominated by multiple bounces and therefore composes a good test environment for SBR [3].

The code is implemented for open scatterers where the aperture chosen for final aperture integration becomes crucial. If the electromagnetic field values on the exit aperture were known exactly, regardless of the chosen exit aperture, exact far field result can be obtained [3]. Plane aperture and conformal aperture (coinciding with the scatterer itself) are implemented for final aperture integration. Results are critically evaluated to choose the best exit aperture to achieve accurate results.

Both for simple and complex targets, geometries are specified in STL mesh format. In STL mesh format, targets are constructed from triangular patches. Corner points and normal vectors of triangular patches are specified in this format. RCS is typically presented in plots of RCS values versus aspect angle. Aspect angle is the angle of target with respect to radar position. Different sweep configurations are implemented in the SBR code. For some cases, the target and receiver are fixed and the transmitter is rotated, for some cases the transmitter and receiver are fixed, and the target is rotated.

### ***1.3 Outline of the Thesis***

The thesis is organized in three main chapters. In Chapter 2 formulation of basic SBR algorithm is discussed. The code is tested over simple test targets like plate, cube, polyhedron and dihedral. Final aperture integration part of the code is discussed in detail and a new approach is developed in Chapter 2. Also, shadowing and multiple scattering are studied in this chapter.

In Chapter 3, application of SBR to complex targets is discussed. Methods of constructing a CAD model are studied. The chapter continues with the sweep definition. RCS of complex targets like ship, aircraft and tank are simulated in this part as well. Results are compared with FEKO results.

The thesis is summarized in Chapter 4. Advantages and disadvantages of the method are discussed. Concluding remarks are made on numerical results. The Chapter terminates with a summary of possible future work where possible modifications/enhancements of the algorithm are discussed.

## **CHAPTER 2**

### **SHOOTING AND BOUNCING RAY METHOD**

In this chapter, the Shooting and Bouncing Ray (SBR) method is discussed. It should be mentioned that the presented algorithm is a ray-based technique which can compute the RCS of electrically large, arbitrarily-shaped Perfect Electric Conductor (PEC) targets. Basically, the algorithm consists of ray tracing, amplitude tracking and final aperture integration parts.

The main blocks of the algorithm are discussed in Section 2.1. In Section 2.3, final aperture integration part of the algorithm is studied in details. Essentially, the algorithm is used to calculate the RCS of open scatterers. So, it is not convenient to perform the ray-tube integration over a common exit plane aperture [6]. SBR algorithm is powerful to calculate multiple scattering effects. In Section 2.4 this attribute of the algorithm is tested over problems dominated by multiple bounce effects. In Section 2.2 numerical results of SBR code are compared with the results of FEKO software. The last section is devoted to the shadowing effect.

## ***2.1 Formulation of the Shooting and Bouncing Ray***

### ***Method***

Shooting and Bouncing Rays (SBR) method is based on ray tracing. The problem is to determine the scattered field from an open scatterer. Basically, rays that simulate the incident plane wave are shot into the target, traced on the target and finally gathered in an exit aperture. Electric field is traced within the rays with Geometric Optic (GO) rules. The algorithm will be discussed in three main parts: 1) ray tracing 2) amplitude tracking and 3) physical optics approximation in exit aperture.

SBR uses both GO and PO rules. Referring to Figure 2.1 consider an arbitrary - shaped PEC object and an incident plane wave.

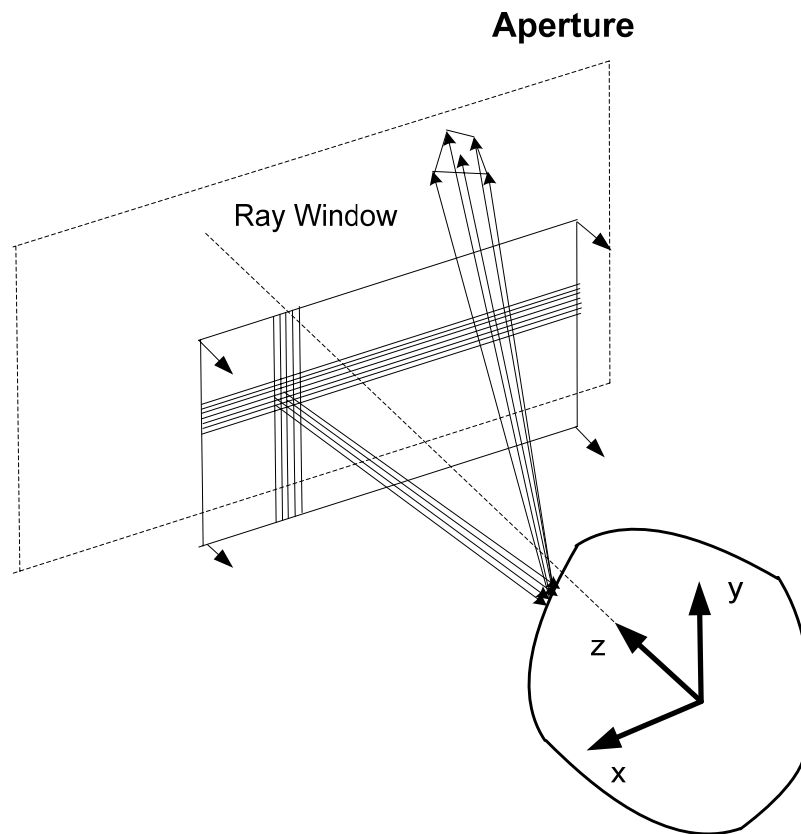


Figure 2.1 SBR, incident rays and exit aperture

The incident plane wave is represented by a dense grid of rays. A ray is defined by an origin,  $P = (x_p, y_p, z_p)$  and a direction vector  $D = (s_x, s_y, s_z)$ . The equation for the ray is;

$$I(t) = P + t\vec{D}, t \geq 0 \quad (2.1)$$

where,

$$s_x = -\sin \theta_i \cos \phi_i \quad (2.2)$$

$$s_y = -\sin \theta_i \sin \phi_i \quad (2.3)$$

$$s_z = -\cos \theta_i \quad (2.4)$$

$\theta_i$  and  $\phi_i$  are angles that denote the direction of incidence.

The defined rays are shot into the PEC object. Let's  $z = f(x, y)$  be the equation of the surface of the scatterer. The intersection points of rays and the surface are found by solving equations of the surface and rays simultaneously. For example, if the object is a plate (i.e. the surface is a plane) we can find the intersection point as follows; a plane can be defined by a normal vector  $N$  and a point on the plane  $Q$ . A point  $P$  is on the plate if:

$$\vec{N}(P - Q) = 0 \quad (2.5)$$

By combining the equations of plane and ray together we end up with the following equation:

$$\vec{N} \times (P + t\vec{D} - Q) = 0 \quad (2.6)$$

where

$$t = \frac{\vec{N}(Q - P)}{\vec{N} \times \vec{D}} \quad (2.7)$$

For simple shapes like plate, sphere or cylinder a single implicit equation is enough to define the shape of the surface. For complex targets, a superposition of triangular patches can be used to approximate the geometry. In this case intersecting a ray with a triangle is more complicated than simple shapes. Basically, ray triangle intersection can be accomplished in two steps;

- Intersecting the ray and the plane of the triangle,
- Checking whether the intersection point is inside or outside the triangle.

Ray-plane intersection is already discussed in equations (2.5), (2.6) and (2.7). After finding the intersection point, we must decide whether the point is inside or outside the triangle. A triangle is defined with three vertices  $p_0$ ,  $p_1$  and  $p_2$ . The normal vector of the triangle ( $n$ ) is defined via the right hand rule.

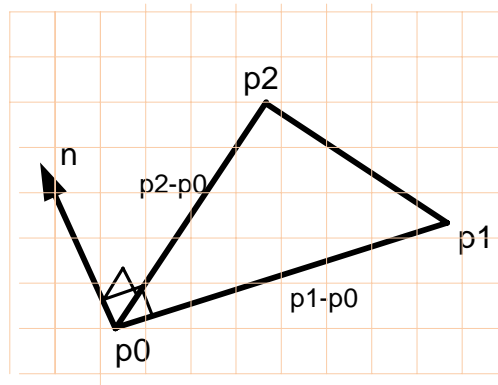


**Figure 2.2 Triangle defined with right hand rule**

$$\hat{n} = (p_1 - p_0) \times (p_2 - p_0) \quad (2.8)$$

A triangle is the intersection of three half spaces as in Figure 2.3. Each edge of the triangle lies on a line and a point is inside the triangle if it is on the correct side of each one of the three lines [9].

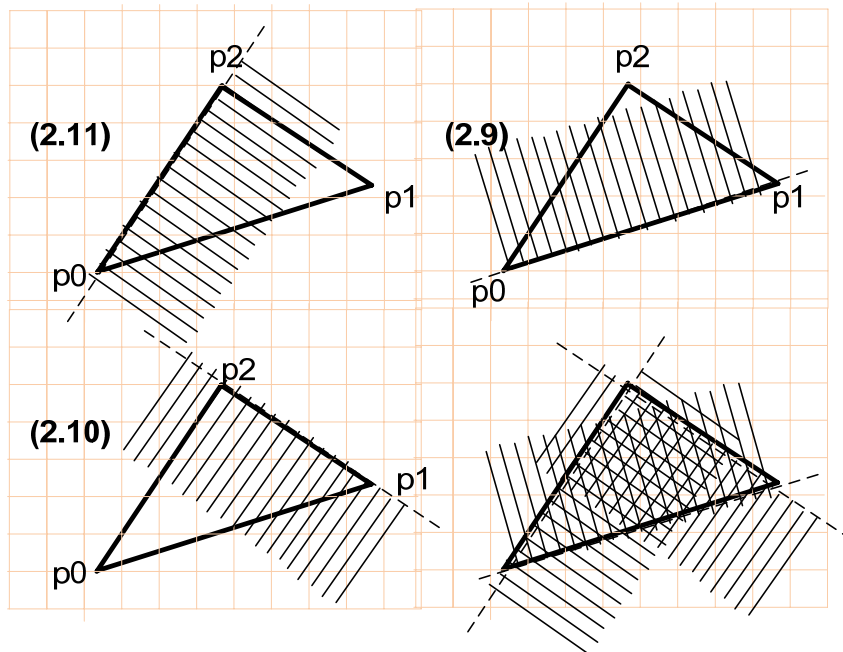


Figure 2.3 A triangle constructed from three half spaces

Using this definition, a point is inside the triangle if it is on the left side of each edge. Via the cross product, it can be decided whether a point  $x$  is on the left or right of the edges with the following equations;

$$((p1 - p0) \times (x - p0)) \cdot \hat{n} \geq 0 \quad (2.9)$$

$$((p2 - p1) \times (x - p1)) \cdot \hat{n} \geq 0 \quad (2.10)$$

$$((p0 - p2) \times (x - p2)) \cdot \hat{n} \geq 0 \quad (2.11)$$

Next, the reflected ray is determined by using the rules of Snell's law [2];

- 1) Reflected ray must lie in the plane of incidence
- 2) The angle of reflection must be equal to the angle of incidence

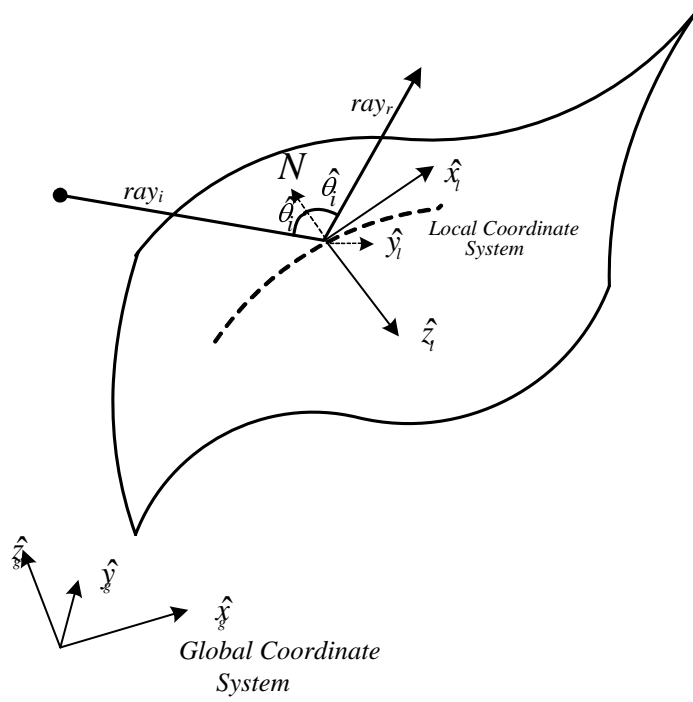


**Figure 2.4 Reflection of a ray**

Referring to Figure 2.4 the reflected ray can be determined according to Snell's law. A unit vector is defined as

$$\hat{m} = (ray_i \times \vec{N}) / \sin \theta_i \quad (2.12)$$

where  $ray_i$  is the incident ray and  $N$  is the reflection normal. Note that  $m$  is perpendicular to the plane of incidence. Referring to Figure 2.4, define the local coordinates

$$y_i = \hat{m} \quad (2.13)$$

$$z_i = -\vec{N} \quad (2.14)$$

$$x_i = -(\hat{m} \times \vec{N}) \quad (2.15)$$

In spherical coordinates  $ray_r$  can be determined as follows

$$ray_r = (r, \theta, \phi) \quad (2.16)$$

$$r = 1, \quad \theta = -(\pi/2 - \hat{\theta}_i), \quad \phi = 0 \quad (2.17)$$

Next,  $(x_l, y_l, z_l)$  coordinates of  $ray_r$  in the local coordinate system can be calculated by spherical to Cartesian coordinate transformation. As a final step local to global coordinate transformation is achieved as below;

$$A = \begin{bmatrix} 1 & 0 & 0 \\ 0 & 1 & 0 \\ 0 & 0 & 1 \end{bmatrix} \quad (2.18)$$

$$C = \begin{bmatrix} x_l(1) & x_l(2) & x_l(3) \\ y_l(1) & y_l(2) & y_l(3) \\ z_l(1) & z_l(2) & z_l(3) \end{bmatrix} \quad (2.19)$$

$$B = A \cdot C^{-1} \quad (2.20)$$

$$(x_g, y_g, z_g) = B \cdot (x_l, y_l, z_l) \quad (2.21)$$

where, B is the transformation matrix. By using the reflected ray as a new incident ray this procedure is applied until the ray ends to bounce in the geometry.

In ray paths the field amplitude is also traced. In Geometrical Optics, the amplitude, phase and polarization of electric field can be updated with the following equation.

$$\vec{E}(x_{i+1}, y_{i+1}, z_{i+1}) = (DF)_i \cdot \Gamma_i \cdot \vec{E}(x_i, y_i, z_i) \cdot e^{-j\phi} \quad (2.22)$$

Where  $\phi = k_0[(x_{i+1} - x_i)^2 + (y_{i+1} - y_i)^2 + (z_{i+1} - z_i)^2]^{1/2}$  and  $DF_i$  is the divergence factor which calculates the spreading of ray tubes. DF is applicable for curved surfaces and for planar surfaces takes the value of 1.  $\Gamma_i$  is the planar reflection

coefficient. For PECs, planar reflection coefficient can be applied with the equation (2.23).

$$\vec{E}_r = (-E_i) + (2(\hat{n} \times \vec{E}_i) \times \hat{n}) \quad (2.23)$$

The scattered far field can be computed by applying the basic physical optics approximation in the aperture where exit rays are gathered. The magnetic current sheet  $\vec{M}_s$  over the aperture is;

$$\vec{M}_s = 2\vec{E}(x, y, z) \times \hat{n}_a \quad (2.24)$$

where,  $\vec{n}_a$  is aperture normal.

From this magnetic current sheet, the scattered field can be calculated. The scattered far field is the sum of contributions from individual ray tubes. The contribution of a ray tube is calculated as;

$$\vec{E}^s = \frac{e^{-jk_0 r}}{r} [\hat{\theta}_i A_\theta + \hat{\phi}_i A_\phi] \quad (2.25)$$

and,

$$\vec{M}_s = [E_{0\theta} \hat{\theta} + E_{0\phi} \hat{\phi}] \times 2\hat{z} \quad (2.26)$$

where,

$$\hat{\phi} = \cos \theta \cos \phi \hat{x} + \cos \theta \sin \phi \hat{y} - \sin \theta \hat{z} \quad (2.27)$$

$$\hat{\theta} = -\sin \phi \hat{x} + \cos \phi \hat{y} \quad (2.28)$$

$$\vec{M}_s = 2E_{0\theta} [\sin(\phi) \hat{y} + \cos(\phi) \hat{x}] + 2E_{0\phi} [-\cos(\theta) \cos(\phi) \hat{y} + \cos(\theta) \sin(\phi) \hat{x}] \quad (2.29)$$

$$A = \frac{jk_0}{4\pi} \iint M_s e^{jk \cdot r} dx dy \quad (2.30)$$

$$A_\theta = \frac{jk_0}{2\pi} \iint_{\Sigma_A} dx dy e^{jk_0(ux+vy)} \cdot [E_x \cos \phi_i + E_y \sin \phi_i] \quad (2.31)$$

$$A_\phi = \frac{jk_0}{2\pi} \iint_{\Sigma_A} dx dy e^{jk_0(ux+vy)} \cdot [(-E_x \sin \phi_i + E_y \cos \phi_i) \cos \theta_i] \quad (2.32)$$

$$u = \sin \theta_i \cos \phi_i \quad (2.33)$$

$$v = \sin \theta_i \sin \phi_i \quad (2.34)$$

For the bistatic case,  $\theta^i$  and  $\phi^i$  values in equations (2.31), (2.32), (2.33) and (2.34) are replaced with observation angles.

Since the outgoing rays are not uniform, the integrations cannot be evaluated easily [2]. At this point, shooting and bouncing ray method has a way out. A small ray tube is shot into the geometry. The ray tube bounces on the geometry and comes to the aperture finally. Then the scattered field is calculated from this ray tube. Enough ray tubes are shot into the geometry to model the incident plane wave. The total scattered field is the sum of all contributions from the ray tubes.

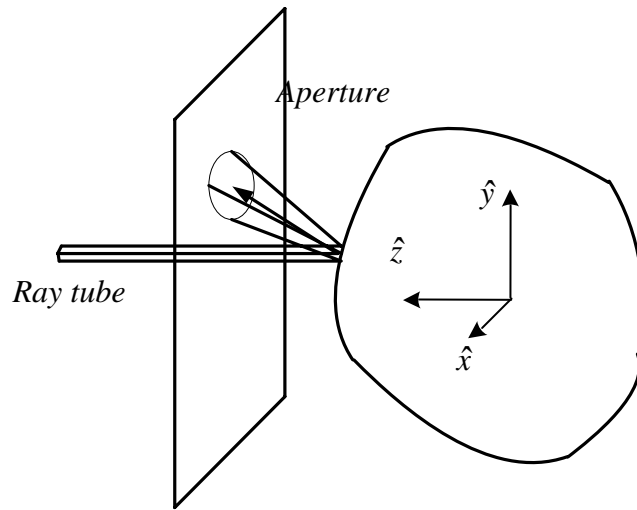


Figure 2.5 Ray tube

Assume that the incident ray tube has an area of  $(\Delta x_0 \Delta y_0)$ . The central ray with direction vector  $(s_x, s_y, s_z)$  hits the aperture. The ray tube will have an area of  $(\Delta x_s \Delta y_s)$  on the aperture and the field within the existing ray tube can be approximated as

$$\begin{bmatrix} E_x(x, y) \\ E_y(x, y) \end{bmatrix} = \begin{bmatrix} E_x(x_i, y_i) \\ E_y(x_i, y_i) \end{bmatrix} e^{-jk_0[s_x(x-x_i)+s_y(y-y_i)]} \quad (2.35)$$

This means that the amplitude of the field is same on the ray tube and across the ray tube there is a linear phase variation [2]. If the size of existing ray tube is too large, the approximation will not be valid. With equations below;

$$A_\theta = \frac{jk_0}{2\pi} \sum_i \iint_{\substack{\text{ray} \\ \text{tube}}} dx dy e^{jk_0(ux+vy)} e^{-jk_0[s_x(x-x_i)+s_y(y-y_i)]} \cdot [E_x(x_i, y_i) \cos \phi^i + E_y(x_i, y_i) \sin \phi^i] \quad (2.36)$$

$$A_\phi = \frac{jk_0}{2\pi} \sum_i \iint_{\substack{\text{ray} \\ \text{tube}}} dx dy e^{jk_0(ux+vy)} e^{-jk_0[s_x(x-x_i)+s_y(y-y_i)]} \cdot [(-E_x(x_i, y_i) \sin \phi^i + E_y(x_i, y_i) \cos \phi^i) \cos \theta^i] \quad (2.37)$$

Since  $E_x(x_i, y_i)$  and  $E_y(x_i, y_i)$  are independent of integral variables they can be taken out of the integral;

$$A_\theta = \frac{jk_0}{2\pi} \sum_i [E_x(x_i, y_i) \cos \phi^i + E_y(x_i, y_i) \sin \phi^i] \cdot e^{jk_0(s_x x_i + s_y y_i)} (\Delta x_i \Delta y_i) I_i \quad (2.38)$$

$$A_\phi = \frac{jk_0}{2\pi} \sum_i [(-E_x(x_i, y_i) \sin \phi^i + E_y(x_i, y_i) \cos \phi^i) \cos \theta^i]$$

$$\cdot e^{jk_0(s_x x_i + s_y y_i)} (\Delta x_i \Delta y_i) I_i \quad (2.39)$$

where

$$I_i = \frac{1}{(\Delta x_i \Delta y_i)} \iint_{\substack{\text{ray} \\ \text{tube}}} dx dy e^{jk_0[(u-s_x)x + (v-s_y)y]} \quad (2.40)$$

The integral in equation (2.40) is the phase factor in standard physical optics theory [3]. Sometimes it is called shape function and it is the Fourier Transform of the ray tube shape.

In order to take advantage of this method for each ray tube, four rays around a central ray are shot into the geometry.

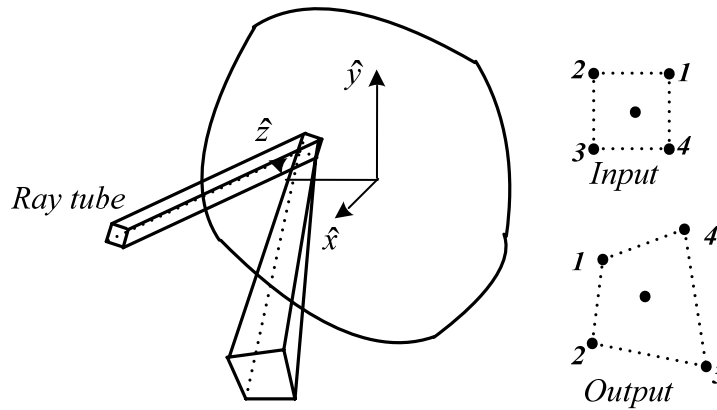


Figure 2.6 Shape of exit ray tube

The position vectors of rays are denoted by  $\vec{\gamma}_n = x_n \hat{x} + y_n \hat{y}$ ,  $n = 1, 2, 3, 4$ . Fourier transform can be evaluated as described in [2], [7]. Simpler proof of this method based on Stokes' theorem can also be considered in [10].

$$I_i = S(p, q) / S(0, 0) \quad (2.41)$$

where,

$$S(p, q) = \sum_{n=1}^4 e^{j\vec{w} \cdot \vec{\gamma}_n} \frac{(x_{n+1} - x_n)(y_n - y_{n-1}) - (y_{n+1} - y_n)(x_n - x_{n-1})}{[(x_n - x_{n-1})p + (y_n - y_{n-1})q][(x_{n+1} - x_n)p + (y_{n+1} - y_n)q]} \quad (2.42)$$

$$S(0, 0) = |(x_1 y_2 - x_2 y_1) + (x_2 y_3 - x_3 y_2) + (x_3 y_4 - x_4 y_3) + (x_4 y_1 - x_1 y_4)| / 2 \quad (2.43)$$

$$p = k_0(u - s_x) \quad (2.44)$$

$$q = k_0(v - s_y) \quad (2.45)$$

$$\vec{w} = p\hat{x} + q\hat{y} \quad (2.46)$$

As a final step, RCS can be calculated as in equations (2.47) and (2.48).

$$RCS = 4\pi \cdot |A_\theta|^2 \quad (\text{Vertical polarization}) \quad (2.47)$$

$$RCS = 4\pi \cdot |A_\phi|^2 \quad (\text{Horizontal polarization}) \quad (2.48)$$

## 2.2 Numerical Results for Simple Targets

In this section, RCS values of some simple targets are compared with Method of Moments (MoM) and Physical Optics (PO) results. FEKO, a software product for the simulation of electromagnetic fields, is used to obtain MoM and PO results. Different solution techniques implemented within FEKO make it applicable for a wide range of problems [5]. The targets of interest are a plate, a cube and a flare-like shape. Generally, monostatic RCS of targets were calculated for vertical polarization. Targets are swept in  $\theta$  angle. FEKO software runs on computers;

Computer 1; Intel (R) Core 2 Duo CPU, E4500@2.20GHz

**3.25GB RAM**

Computer 2; (Dual) AMD Opteron™ Processor 248

**14.926 GB RAM**

Computer 2 is used for electrically large problems. Even with computer 2 some problems cannot be solved with MoM. Multilevel Fast Multipole Method (MLFMM) which is a fast alternative formulation of the MoM is applicable to much larger structures than the MoM [5]. MLFMM makes it possible to obtain full-wave solutions for electrically large structures [5]. With this method and computer 2, a military aircraft at 2.5GHz or a ship at 400MHz can be handled. In order to solve the same problems with MoM, we need 30TByte memory approximately.

Different sweep geometries are used to calculate the RCS values of simple PEC obstacles. In the plate geometry, plane wave (provided by the transmitter) is swept around the target in  $\theta$  angle and plate is kept fixed in origin. For cube and flare like shape, transmitter and exit aperture (in the direction of the receiver) are kept fixed and the target is rotated in  $y$  axis. Both approaches can be used to calculate the monostatic RCS.

The plate geometry is formulated in the problem directly by using its equation. The cube and flare like geometry are created from triangle patches that are big enough to permit to construct these shapes. The number of the triangular patches is kept minimal to decrease the runtime since the SBR code generated in MATLAB does not include a special algorithm that speeds up the ray-triangle intersection test. Ray-triangle intersection is tested with brute force methods, which implies that runtime increases dramatically with the number of patches.

The first simulation was conducted on a perfect electric conductor (PEC) flat plate as illustrated in Figure 2.7. In this simulation both monostatic and bistatic RCS of a square PEC plate with side length of 0.25 meters were computed and compared with MoM and PO results taken from FEKO.

The plate was illuminated from  $\phi = 0^\circ$  and  $\theta = 0^\circ$  and its monostatic RCS was computed with respect to frequency from 2GHz to 6GHz as shown in Figure 2.7. The result of the SBR is compared with the MoM and given in Figure 2.8.

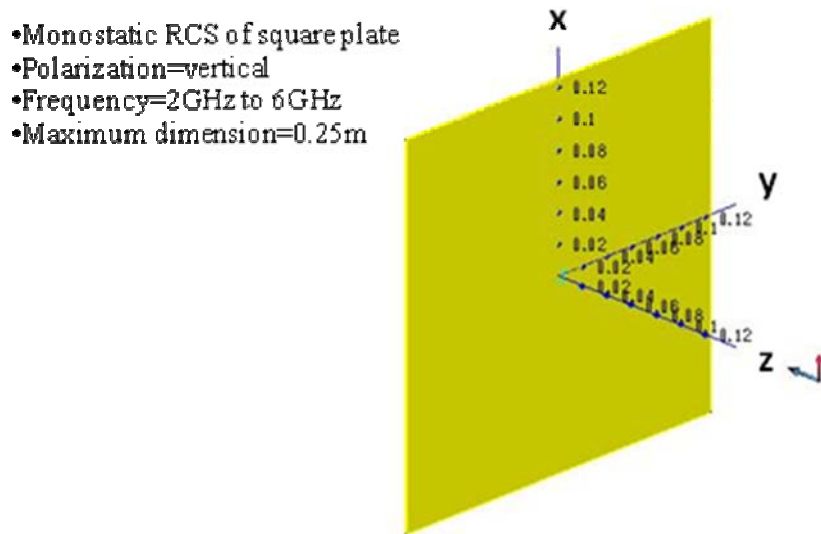


**Figure 2.7 Simulation setup for monostatic RCS of PEC plate**

Rays are shot towards the plate with  $\lambda/10$  density, where  $\lambda$  is wave length. For each ray, four rays neighboring the central ray are shot to build up a ray tube. Since specular reflections are dominant, the results of SBR solution and MoM are perfectly matched.

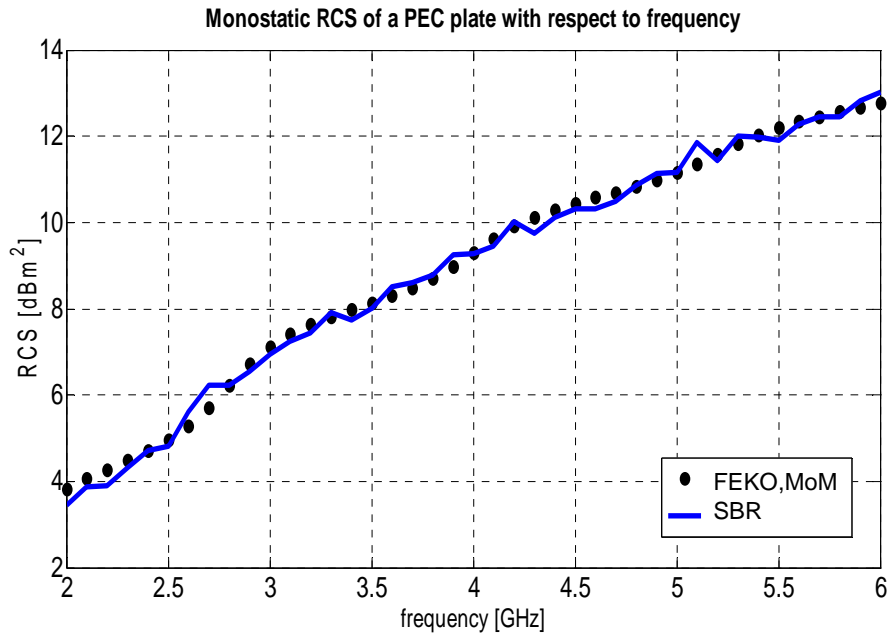


**Figure 2.8 Comparison of MoM and SBR results for  $\theta\theta$  polarized monostatic RCS of PEC plate with respect to frequency**

For bistatic case, the plate is illuminated from  $\phi = 0^\circ$  and  $\theta = -10^\circ$  and its bistatic RCS is computed at  $\phi = 0^\circ$  and  $\theta = 10^\circ$  with respect to frequency from 2GHz to 6GHz as shown in Figure 2.9. The result of the SBR was compared with the MoM and given in Figure 2.10.

- Bistatic RCS of square plate
- Polarization=vertical
- Frequency=2GHz to 6GHz
- Maximum dimension=0.25m

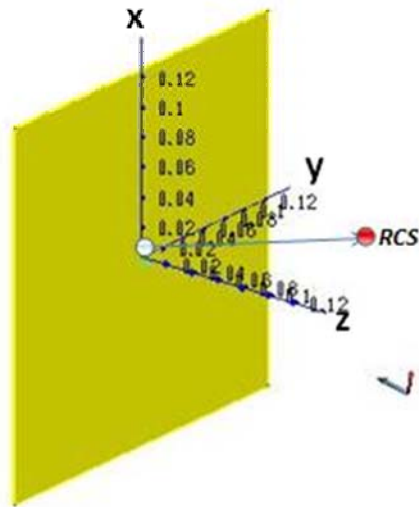


Figure 2.9 Simulation setup for bistatic RCS of PEC plate

As a result for flat surfaces in specular regions the results are matching with MoM results perfectly for both monostatic and bistatic cases.

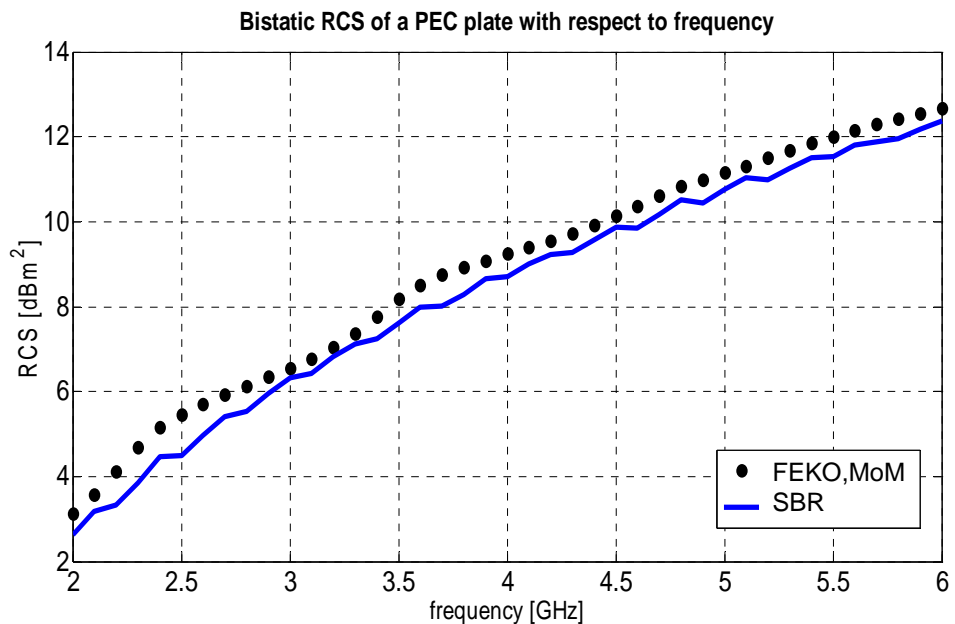


Figure 2.10 Comparison of MoM and SBR results for  $\theta\theta$  polarized bistatic RCS of PEC plate with respect to frequency

In the following example, the plate is illuminated at  $\phi = 0^\circ$  from  $\theta = -60^\circ$  to  $\theta = 60^\circ$  and its monostatic RCS is computed Figure 2.11. The result of the SBR was compared with the MoM in Figure 2.12 and with PO in Figure 2.13.

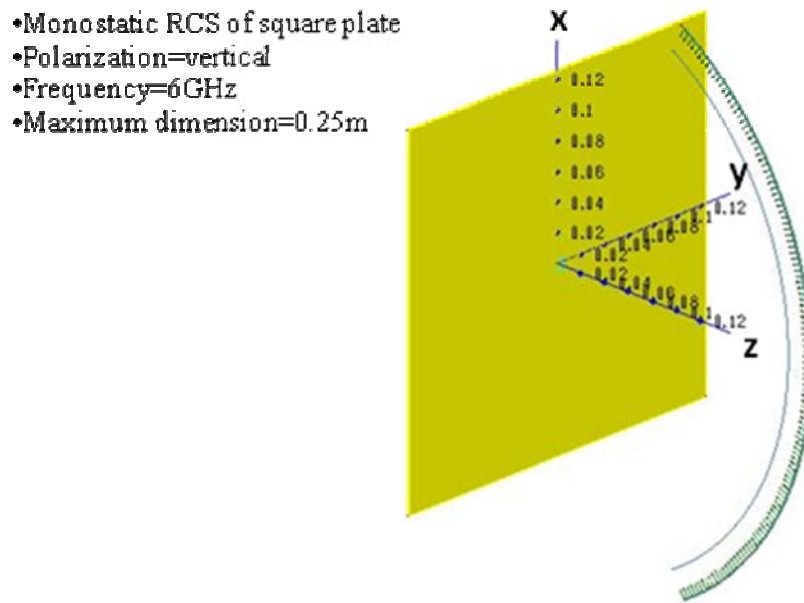
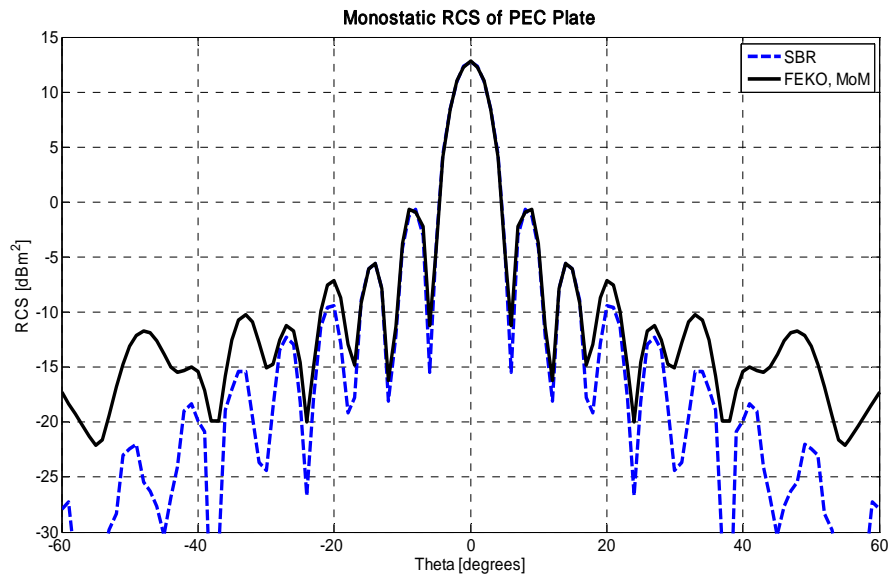
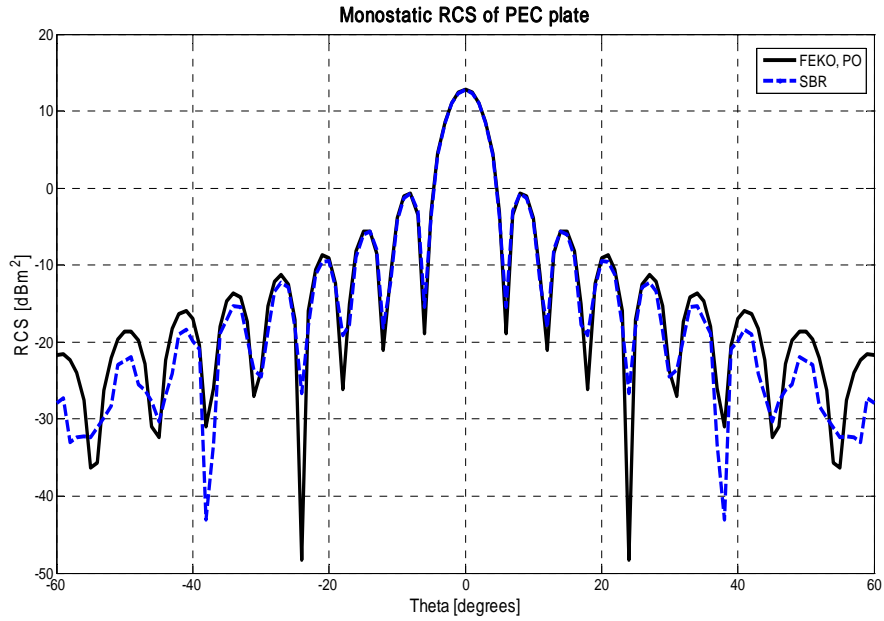


Figure 2.11 Simulation setup for monostatic RCS of PEC plate



**Figure 2.12 Comparison of MoM and SBR results for  $\theta\theta$  polarized monostatic RCS of PEC plate**

The results are perfectly matching with MoM near specular region. Results are not agreeing at angles where diffraction effects are dominant. SBR code is unable to model diffraction. When we compare the results with PO code in FEKO we can see that the results are in good agreement, since PO is also unable to take diffraction into account.



**Figure 2.13 Comparison of PO and SBR results for  $\theta\theta$  polarized monostatic RCS of PEC plate**

In the other case the plate is illuminated from  $\phi = 0^\circ$  and  $\theta = 0^\circ$  and its bistatic RCS is computed at  $\phi = 0^\circ$  from  $\theta = -90^\circ$  to  $\theta = 90^\circ$  as in Figure 2.14. The result of the SBR was compared with the MoM and given in Figure 2.15.

- Bistatic RCS of square plate
- Polarization=vertical
- Frequency=6GHz
- Maximum dimension=0.25m

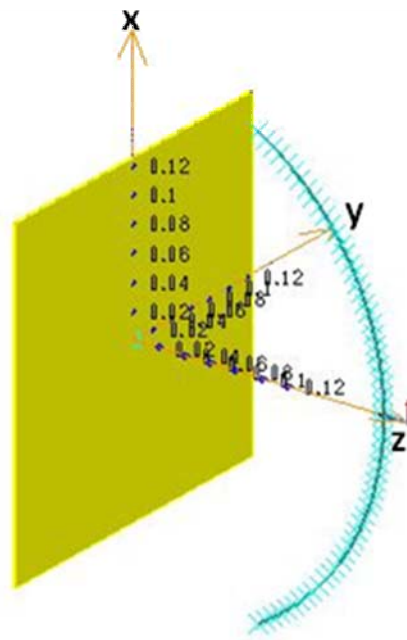
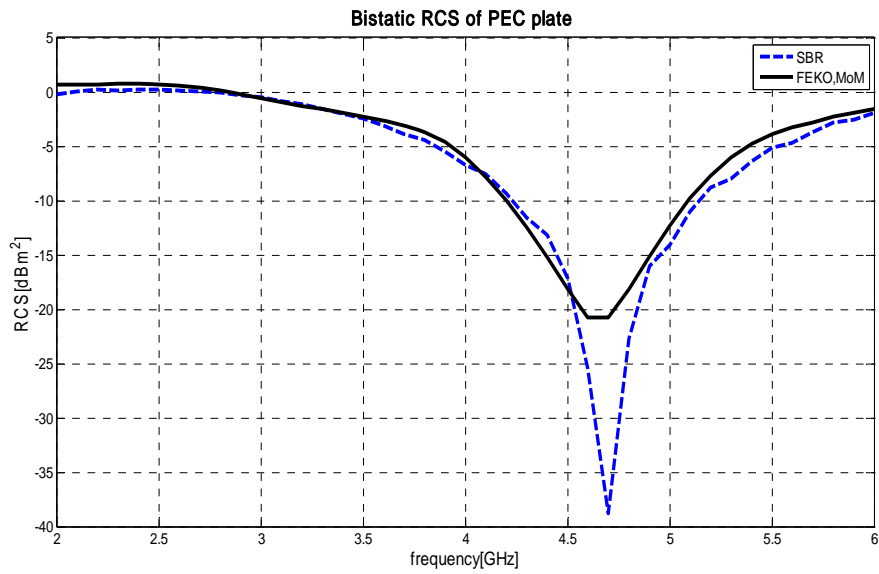


Figure 2.14 Simulation setup for bistatic RCS of PEC plate

The results are harmonious with MoM near specular regions. In rear sides where diffraction contribution is important, the results are not matching well with the MoM results.



**Figure 2.15 Comparison of MoM and SBR results for  $\theta\theta$  polarized bistatic RCS of PEC plate**

Finally, for the plate case, bistatic RCS is computed with respect to frequency. The plate is illuminated from  $\phi = 0^\circ$  and  $\theta = 0^\circ$ , RCS values are computed at  $\phi = 0^\circ$  and  $\theta = 15^\circ$  with respect to frequency from 2GHz to 6GHz as shown in Figure 2.16. The result of the SBR was compared with the MoM and given in Figure 2.17.

- Bistatic RCS of square plate
- Polarization=vertical
- Frequency=2GHZ to 6GHz
- Maximum dimension=0.25m

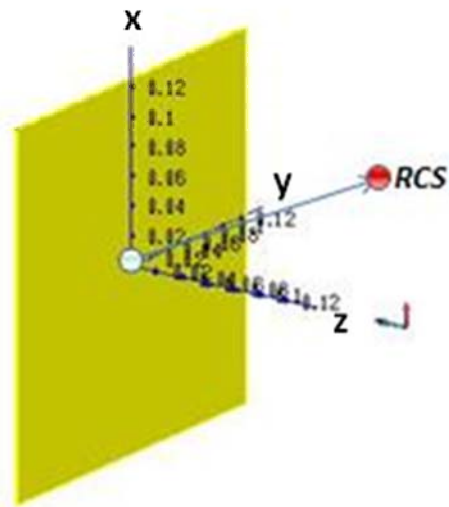
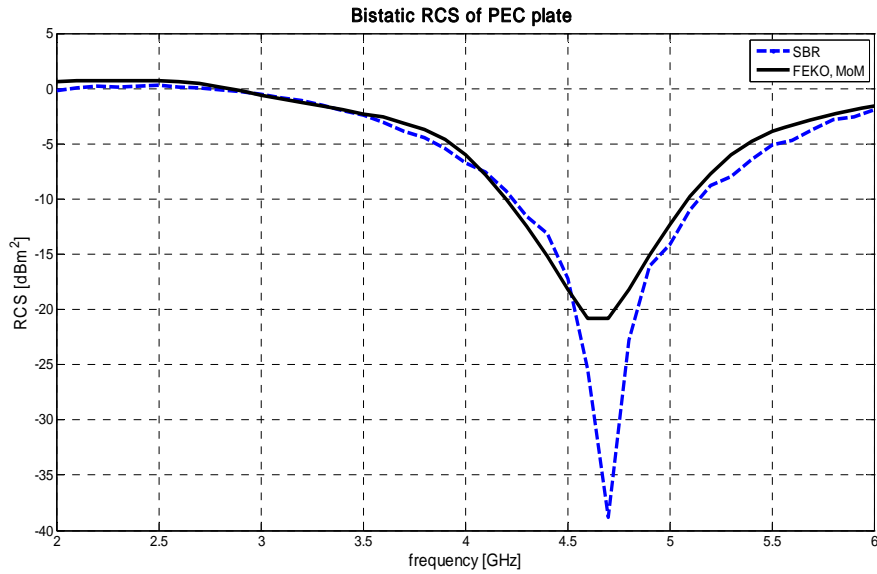


Figure 2.16 Simulation setup for bistatic RCS of PEC plate

Out of the specular region where diffraction mechanism is effective, again the results are not in agreement with MoM results. Hence, it can be concluded that by correctly modeling the diffraction effects, more accurate results can be obtained out of specular regions.



**Figure 2.17 Comparison of MoM and SBR results for  $\theta\theta$  polarized bistatic RCS of PEC plate with respect to frequency**

The second example was conducted on a flare like object shown in Figure 2.18. The object is represented by 20 triangle patches. Maximum length of the object is 0.5 meter. The monostatic RCS is calculated at  $\phi = 0^\circ$  from  $\theta = 0^\circ$  to  $\theta = 180^\circ$  for vertical polarization at 6GHz. For each monostatic RCS value 72000 rays are traced with  $\lambda/10$  density. Results are compared with the PO solution in Figure 2.19.

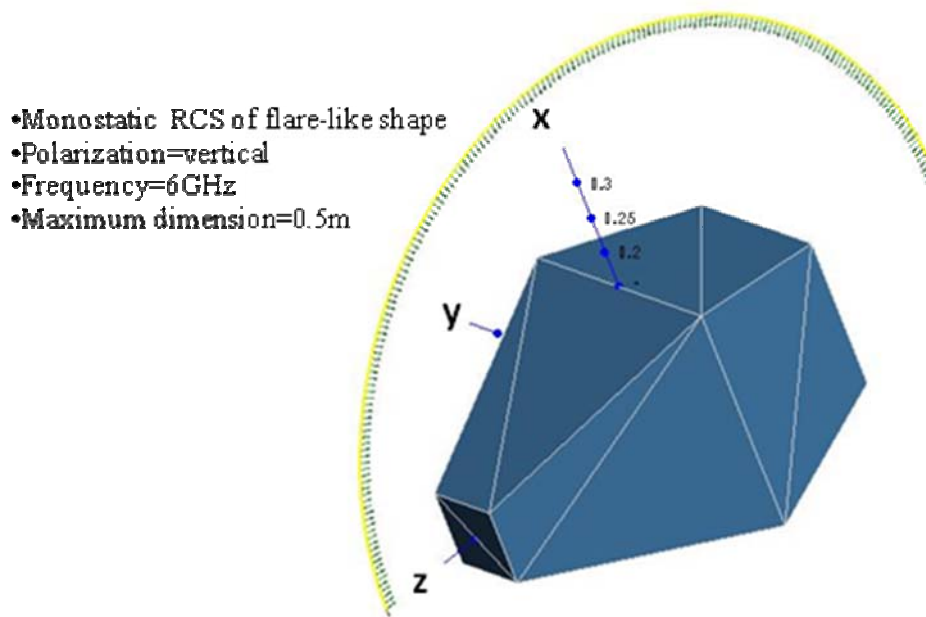
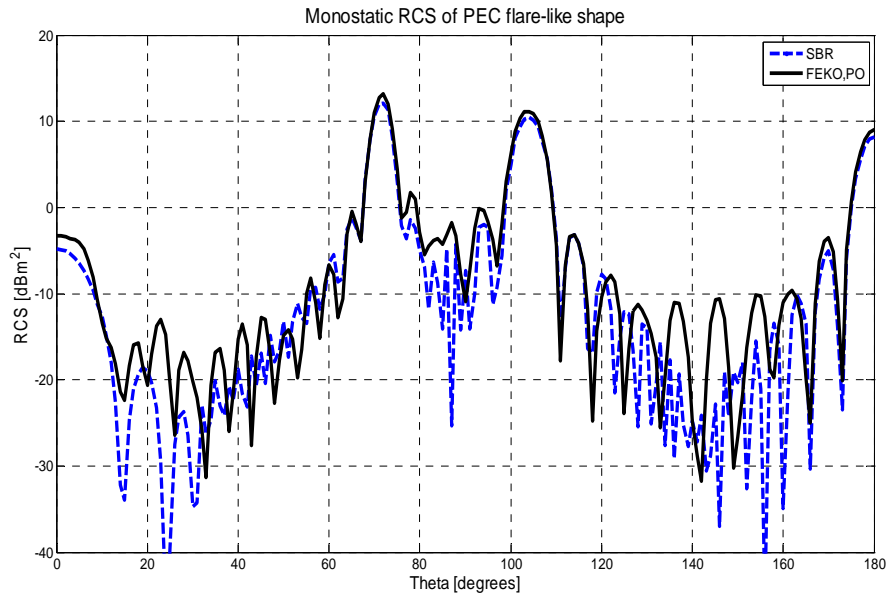


Figure 2.18 Simulation setup for monostatic RCS of PEC flare-like shape

For the angle ranges  $15^\circ < \theta < 50^\circ$ ,  $80^\circ < \theta < 90^\circ$  and  $120^\circ < \theta < 160^\circ$ , the RCS values are not matching with PO results. This discrepancy between the results is due to the shape of the aperture over which the rays are collected. At these angles, some of the rays bouncing from the geometry cannot be gathered at the planar exit aperture. After a detailed analysis, it is seen that the aperture shape must be modified in order to obtain correct results. Alternative solution suggestions and formulations related to this point are considered in Section 2.3. In this section, it will be shown that conformal apertures that encompass the scatterer are effective in collecting rays in a proper fashion. Although this point will be fully clarified in the next section, corrected results obtained by a conformal aperture are represented in Figure 2.20. With this new formulation that will be presented in Section 2.3, results agree very well with the PO solution.



**Figure 2.19 Comparison of PO and SBR results for  $\theta\theta$  polarized monostatic RCS of PEC flare-like shape for planar aperture case**

Results in Figure 2.20 show that SBR algorithm gives the same results as PO solution. Additionally, ray tracing capability of the code handles the multiple scattering and shadowing problems.

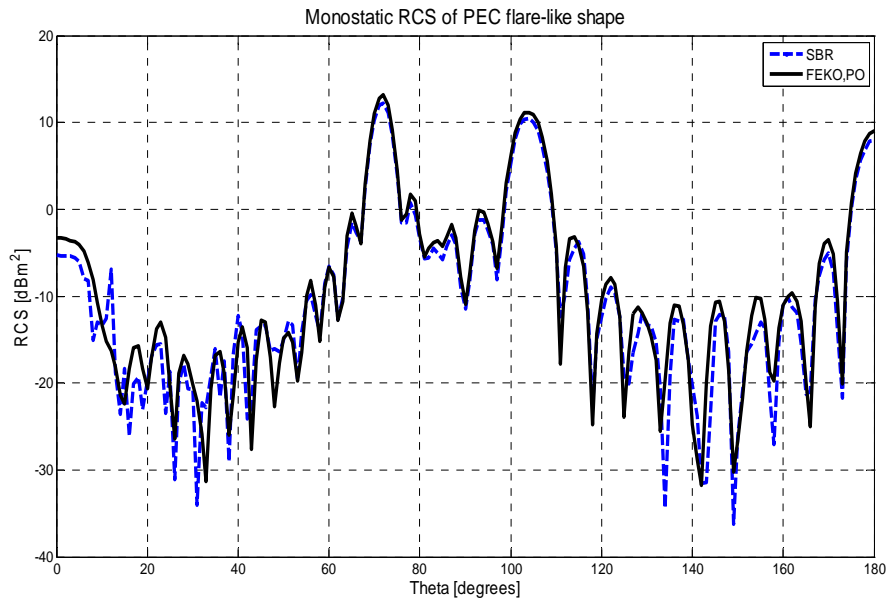


**Figure 2.20 Comparison of PO and SBR results for  $\theta\theta$  polarized monostatic RCS of PEC flare-like shape for conformal aperture case**

The third example was conducted on an arbitrary prism shown in Figure 2.21. The shape is composed of 14 triangular patches. The maximum length of the shape is 0.35 meters. Monostatic RCS is calculated at  $\phi = 0^\circ$  from  $\theta = 0^\circ$  to  $\theta = 360^\circ$  for vertical polarizations at 5GHz. The results are compared with PO and MoM results.

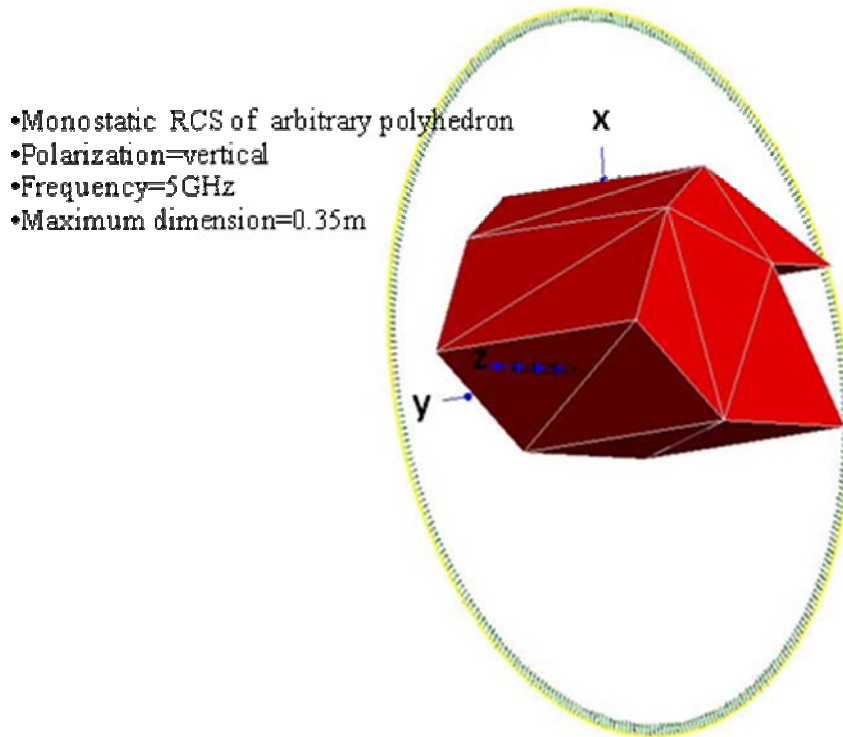


Figure 2.21 Simulation setup for monostatic RCS of PEC arbitrary polyhedron

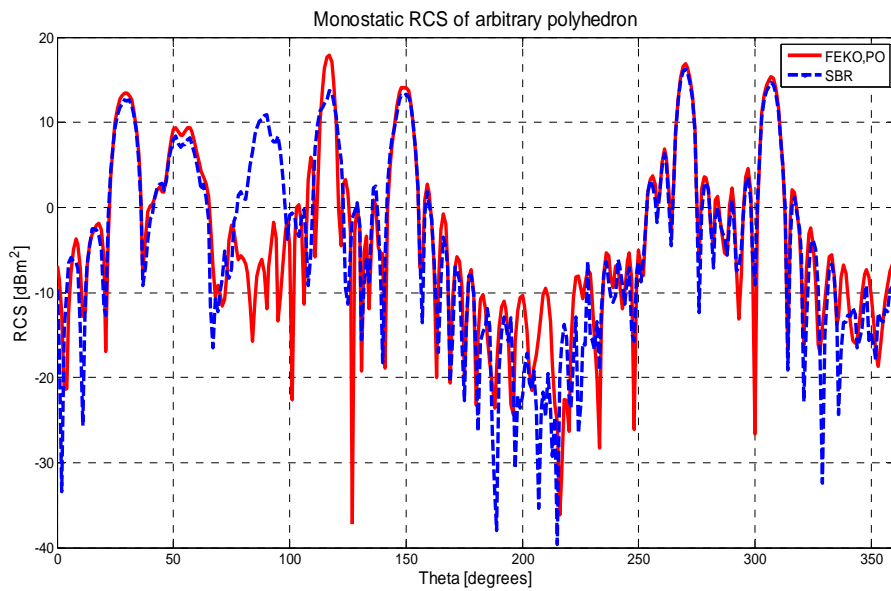
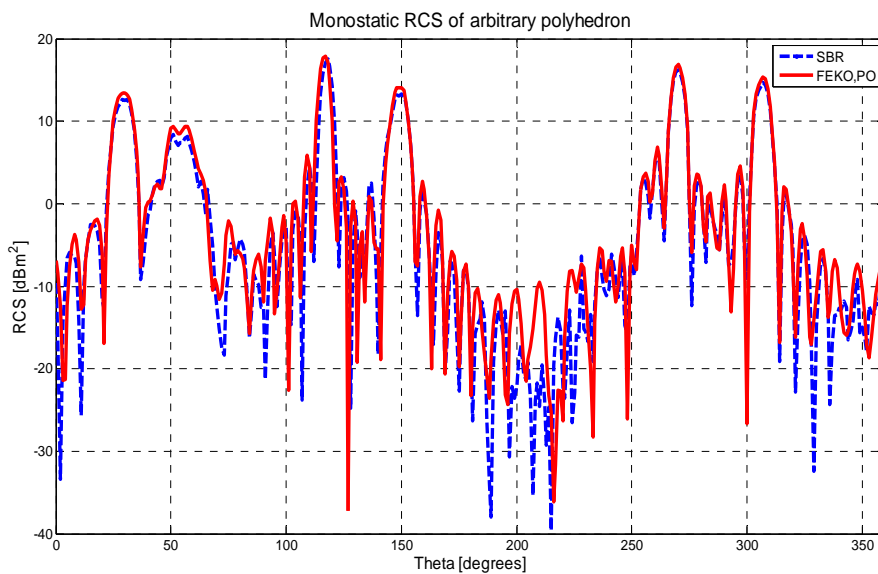


Figure 2.22 Comparison of PO and SBR results for  $\theta\theta$  polarized monostatic RCS of PEC arbitrary polyhedron

In Figure 2.22, it is seen that the results are close to the PO solution except for angles from  $\theta = 60^\circ$  up to  $\theta = 130^\circ$ . The problem at these angles can be revealed when the geometry is investigated more closely in Figure 2.24. At problematic aspect angles, rays that are shot towards the geometry are intersecting with four points located on the surface. The naive ray tracing algorithm of the code is unable to handle such situations, where the object is concave and a ray may intersect with several points on the surface. In section 2.5, it is explained how the algorithm is overviewed to overcome this problem. SBR is a ray tracing method and naturally ray tracing algorithms may correctly handle the shadowing problem. Although the modifications introduced in the code are explained in Section 2.5, the correct results obtained after these amendments are shown in Figure 2.23.



**Figure 2.23 Comparison of PO and SBR results for  $\theta\theta$  polarized monostatic RCS of PEC arbitrary polyhedron after correction on shadowing algorithm**

After these modifications on the code, the results agreed with the PO solution except at angles  $190^\circ < \theta < 230^\circ$ . At these angles, multiple scattering is dominant.

For this example, multiple scattering is not implemented in the code. The results are also compared with the MoM results. In Figure 2.25, multiple scattering effects can be seen in MoM results in an obvious fashion. Multiple scattering effects will be implemented in Section 2.4.

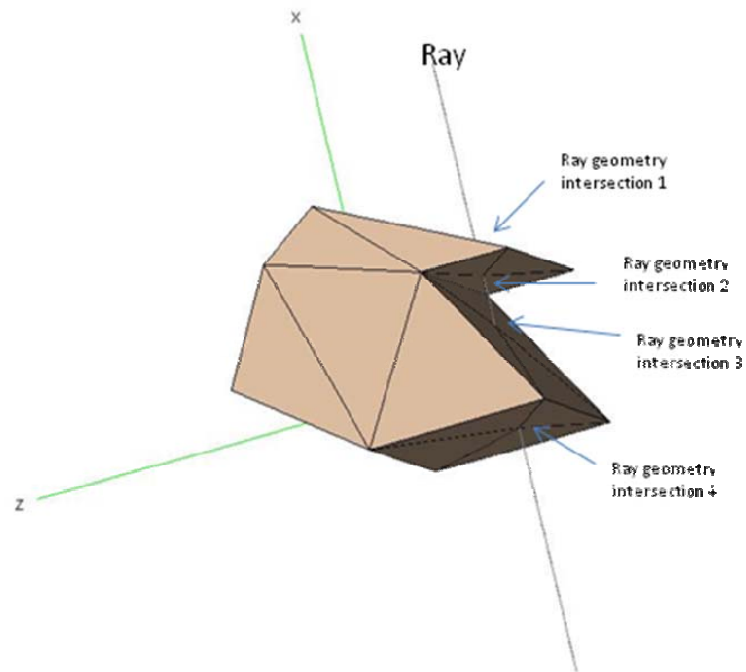


**Figure 2.24 Shadowing effect**

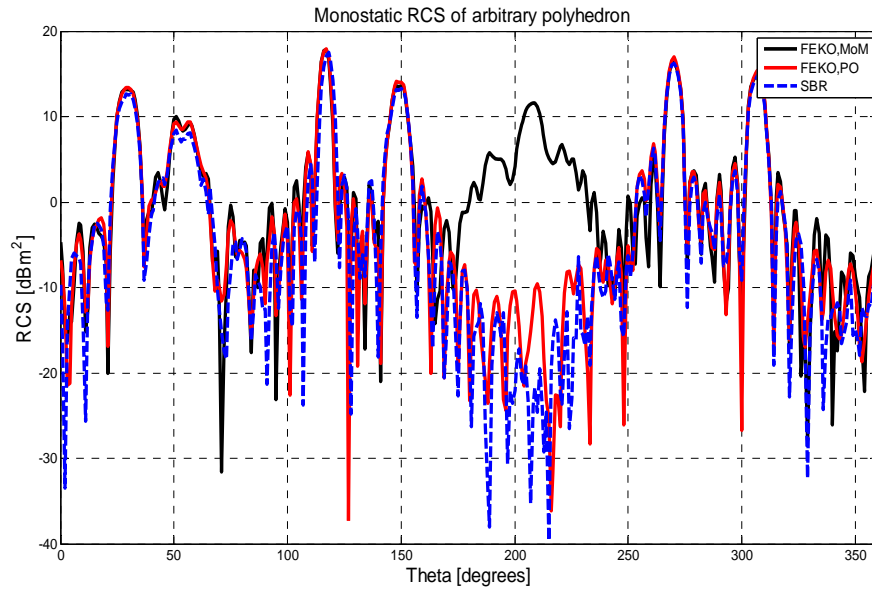


**Figure 2.25 Comparison of PO, MoM and SBR results for  $\theta\theta$  polarized monostatic RCS of PEC arbitrary polyhedron**

The fourth example was conducted on an arbitrary polyhedron shown in Figure 2.26. The shape is composed of 8 triangular patches. The maximum length of the shape is 0.3 meters. The monostatic RCS is calculated at  $\phi = 0^\circ$  from  $\theta = 0^\circ$  to  $\theta = 180^\circ$  for vertical polarizations at 5GHz. The results are compared with PO and MoM results.

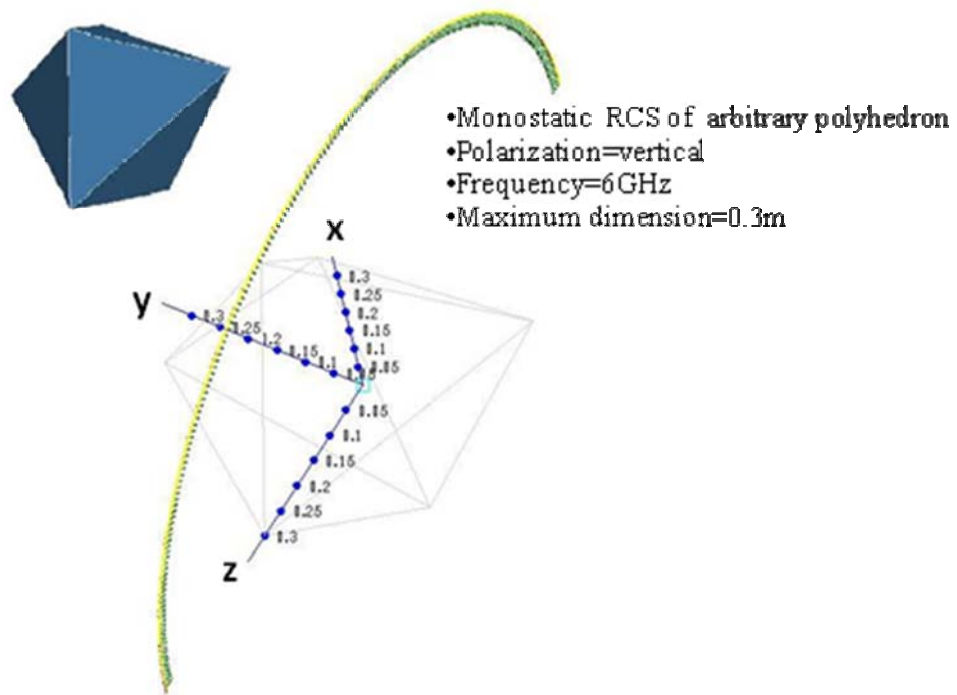


Figure 2.26 Simulation setup for monostatic RCS of PEC arbitrary polyhedron

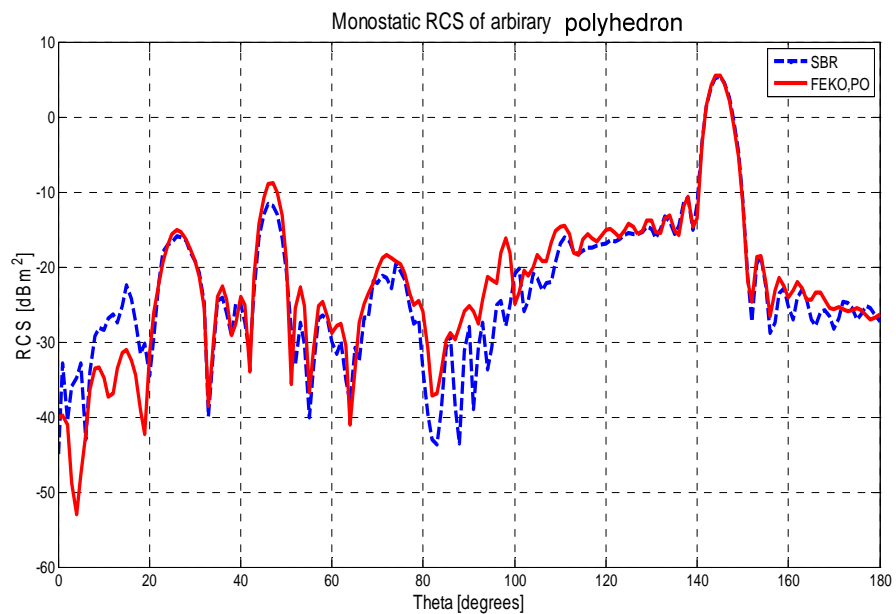
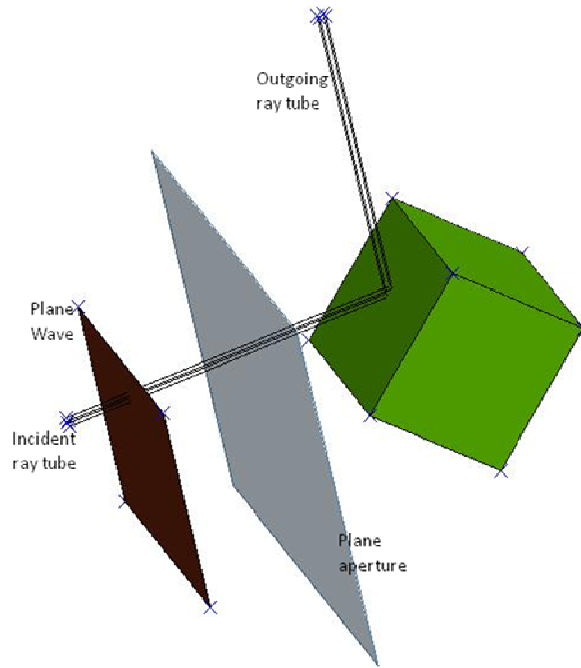


Figure 2.27 Comparison of PO and SBR results for  $\theta\theta$  polarized monostatic RCS of PEC arbitrary polyhedron

The results agree very well with the PO solution for this arbitrary polyhedron. The main reason for this conclusion is the convex shape of the object that avoids all the difficulties encountered in the previous example.

### ***2.3 SBR Final Integration Aperture***

The Shooting and Bouncing Ray method has been first applied on cavity structures like a jet inlet or an aircraft cabin [2], where open mouth of the cavity has been chosen as the final integration aperture. However, for open scatterers there are several options for the choice of an aperture choose. If the exit aperture is chosen as planar, this choice gives good results in specular regions. A planar aperture cannot be adequate for gathering the exit rays for some problems. Basically, the problem can be investigated by using the cube geometry shown in Figure 2.28. With a planar exit aperture, it is not possible to collect outgoing rays at angles close to 45 degrees. By fixing the transmitter (plane wave) and exit aperture (receiver) and rotating the geometry, the monostatic RCS of the cube can be calculated as shown in Figure 2.29.



**Figure 2.28 Planar exit aperture approach**

At angles  $0^\circ < \theta < 30^\circ$ ,  $60^\circ < \theta < 120^\circ$  and  $150^\circ < \theta < 180^\circ$  the results are in good agreement with both MoM and PO results. On the other hand, at angles between  $30^\circ < \theta < 60^\circ$  and  $120^\circ < \theta < 150^\circ$  the field values are well below those obtained by MoM and PO. At  $45^\circ$  SBR code yields  $-\infty$  value. If the MoM and PO results are evaluated together, the difference between them in these problematic angles is not much. So, it can be stated that the problem is not due to the absence of diffraction effect in the code. At angles near  $45^\circ$  the rays bouncing from cube cannot be gathered at the planar aperture. This leads us to state that contribution of rays at these angles are greater than diffraction effects, and their contribution to the RCS value must be taken into account. To overcome this problem, a new exit aperture is recommended and formulated.

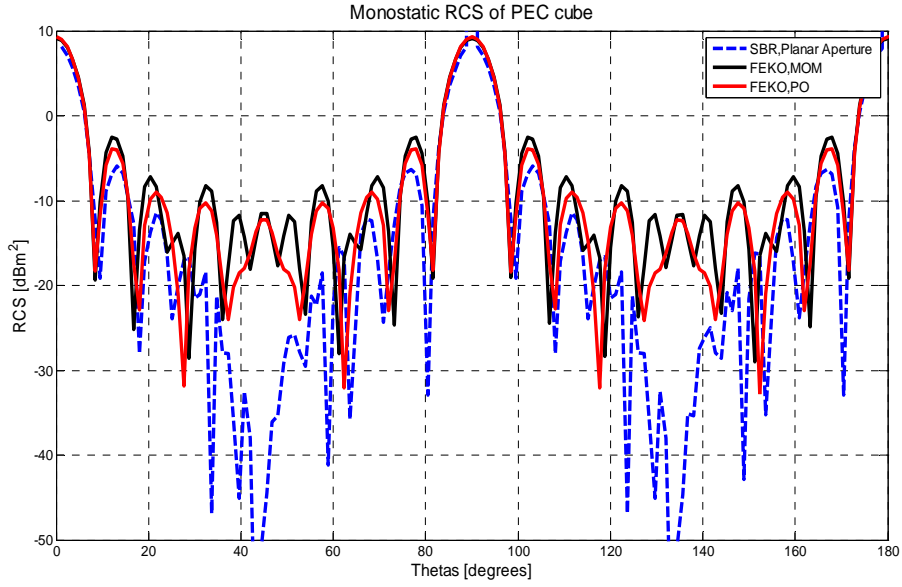


**Figure 2.29 Monostatic RCS of PEC cube with planar exit aperture approach**

A conformal exit aperture as shown in Figure 2.30 can be the best choice to gather the exit rays. In conformal exit aperture, all outgoing rays are gathered and their contributions to overall RCS value can be calculated. Basically, the conformal exit aperture is a replica of the geometry of the surface itself. This guaranties that all rays bouncing from the geometry can be evaluated for their contribution to RCS.

Formulation of a conformal exit aperture is more complicated than a planar exit aperture formulation [8]. In order to simplify the resulting equations, for each element (planar part) of the conformal exit aperture, a local coordinate system  $(x_l, y_l, z_l)$  shall be defined as shown in Figure 2.30. The local coordinates are defined using the following equations;

$$z_l = N \tag{2.49}$$

$N$  is the normal of the triangular patch with which the rays intersect. To define a local coordinate system, local  $z$  coordinate is projected into global  $x, y$  plane according to the following equation;

$$u = z_l - (z_l \cdot a_z)a_z \quad (2.50)$$

Then, to find the global-to-local transformation matrix, rotation angles  $\phi$  and  $\theta$  are calculated by means of equations (2.51) and (2.52).

$$\phi = \cos^{-1}(a_x \cdot u / \|u\|) \quad (2.51)$$

$$\theta = \cos^{-1}(a_z \cdot N / \|N\|) \quad (2.52)$$

The global-to-local transformation matrix can be defined through the multiplication of rotation matrices.

$$\bar{T} = \begin{bmatrix} \cos(\phi) & -\sin(\phi) & 0 \\ \sin(\phi) & \cos(\phi) & 0 \\ 0 & 0 & 1 \end{bmatrix} \times \begin{bmatrix} \cos(\theta) & 0 & \sin(\theta) \\ 0 & 1 & 0 \\ -\sin(\theta) & 0 & \cos(\theta) \end{bmatrix} \quad (2.53)$$

After defining the local coordinate system values in equation (2.42) and (2.43), are transformed into local coordinate system. Then, the incident field given in the global coordinate system is transformed into the local coordinate system as follows:

$$E^i(x_l, y_l, z_l) = E^i(x_g, y_g, z_g) \cdot \bar{T} \quad (2.54)$$

Finally,  $\phi$  and  $\theta$  parameters in equation (2.51) and (2.52) are used in equations (2.31) and (2.32).

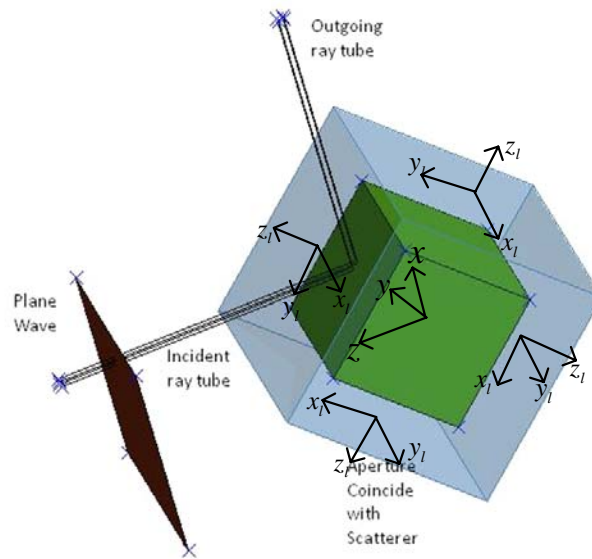


**Figure 2.30 Conformal exit aperture approach**

With aperture modification, at angles between  $30^\circ < \theta < 60^\circ$  and  $120^\circ < \theta < 150^\circ$  the calculated values agree well with MoM and PO results as shown in Figure 2.31.

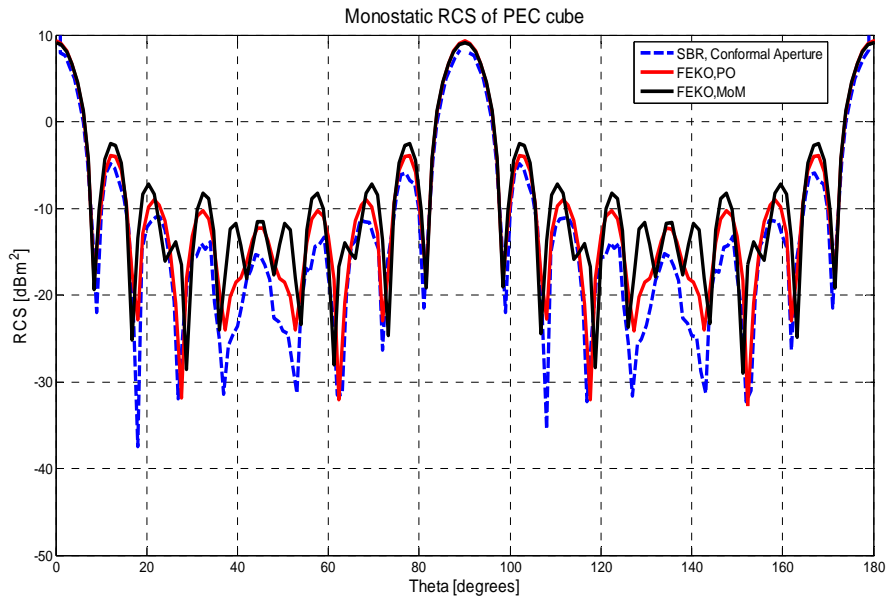


Figure 2.31 Monostatic RCS results with conformal exit aperture approach

## 2.4 SBR Multiple Scattering Capability

In the SBR code, rays must be allowed to bounce within the geometry until they exit. The structure of the algorithm allows us to compute multiple scattering effects without a limit unless we have extremely long runtimes. With non-convex targets that have concave surfaces such as cavities and corners, numerical results of PO deviate from our simulation results. Targets like dihedral and trihedral are appropriate to test the code for multiple scattering capabilities.

A PEC dihedral shown in Figure 2.32 will be a good test object for SBR code. Clearly, scattering from a dihedral is dominated with multiple scattering effects. As shown in Figure 2.32 a dihedral is illuminated from  $\theta = -60^\circ$  to  $\theta = 60^\circ$  and its monostatic RCS was computed with respect to  $\theta$  at 6GHz.

- Monostatic RCS of dihedral
- Polarization=vertical
- Frequency=6 GHz
- Maximum dimension=0.1m

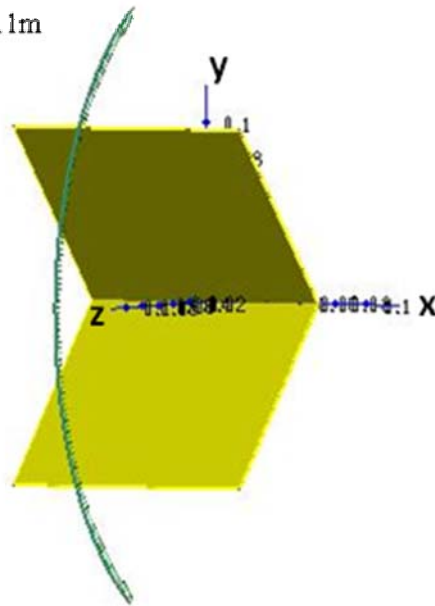


**Figure 2.32 Simulation setup for monostatic RCS of PEC dihedral**

In Figure 2.33 results are obtained with and without considering the multiple scattering effects. Clearly, the RCS values for a problem where multiple scattering is dominant are not matching with MoM results when multiple scattering is not modeled in the code.

The SBR RCS values are in good agreement with the MoM results when multiple scattering mechanism is implemented in the code.

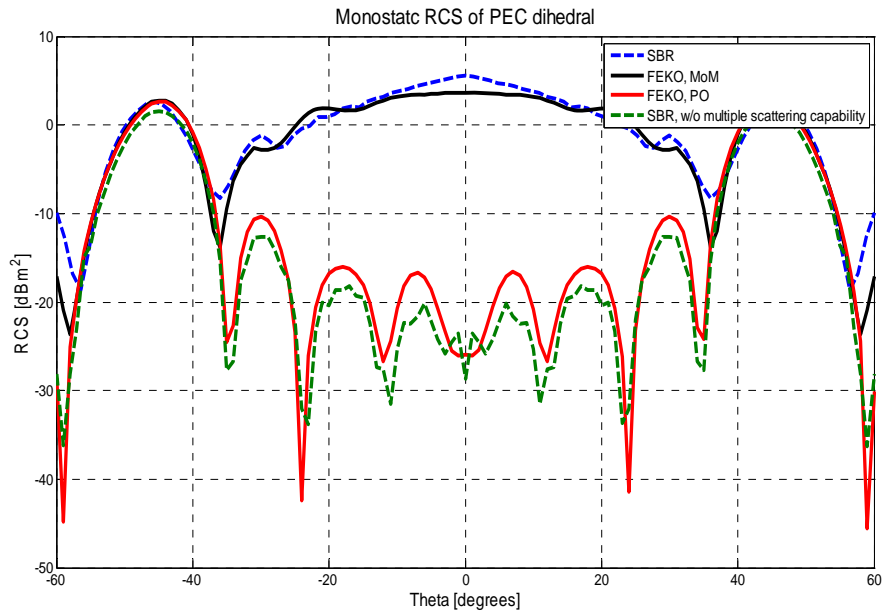


Figure 2.33 Comparison of PO, MoM and SBR results for  $\theta\theta$  polarized monostatic RCS of PEC dihedral

## 2.5 Shadowing

For a specific aspect angle, the incident electromagnetic wave illuminates some parts of the target and the rest of the target will stay in dark. In addition, some parts of the target can be shadowed by other parts of the target itself. Especially, concave and separated parts of targets cause shadowing. For example, wings of airplanes induce shadowing from certain aspect angles over the body of the aircrafts. Many algorithms are developed to solve this problem for the PO approach.

Naturally, SBR is using the ray tracing method, which handles the shadowing effect in a natural way. Basically, if a ray intersects with a part of the target for

the first time, this part will be the illuminated part and the rest will stay in the shadow region.

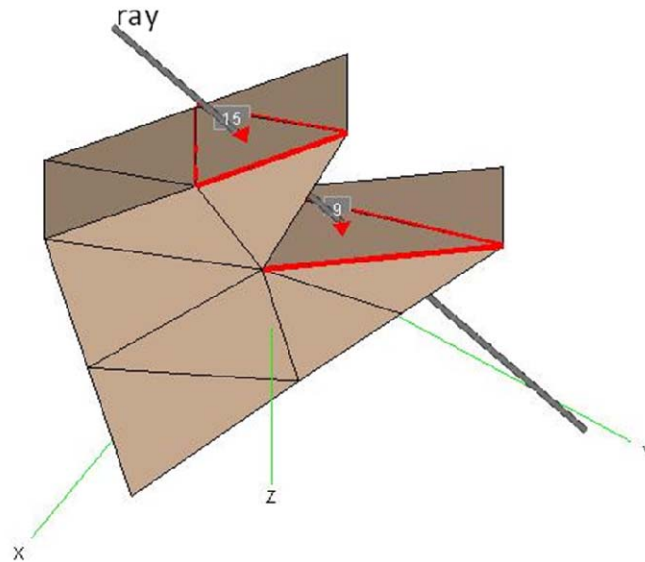


**Figure 2.34 Shadowing problem**

In Figure 2.34, triangle 9 is shadowed by triangle 15. The ray intersects first triangle 15 which is taken as the illuminated part. As a summary, ray tracing is itself a natural shadowing algorithm. Ray tracing is implemented to find the ray-triangle intersection points, and the primary intersection part is taken as the illuminated part, and the rest are assumed to lie in shadow.

## **CHAPTER 3**

### **APPLICATION OF SBR TO COMPLEX TARGETS**

In the previous chapter, the SBR code is tested by using simple PEC objects. However, realistic targets possess much more complex geometries with several scattering mechanisms. The interactions between parts of complex geometries will affect dramatically the RCS values. At this point the SBR code, with its multiple scattering capability, will be superior to other ray based RCS prediction tools. The RCS prediction code developed in the previous chapter will be applied to complex targets in this chapter, in order to evaluate the performance of the method for realistic cases.

In our simulations, targets are modeled using large triangular patches. In order to calculate the monostatic RCS of a target from different aspect angles, two different methods are used. In the first method, the target kept fixed and the ray window in Figure 3.1 is rotated. This method is applied to simple shapes.

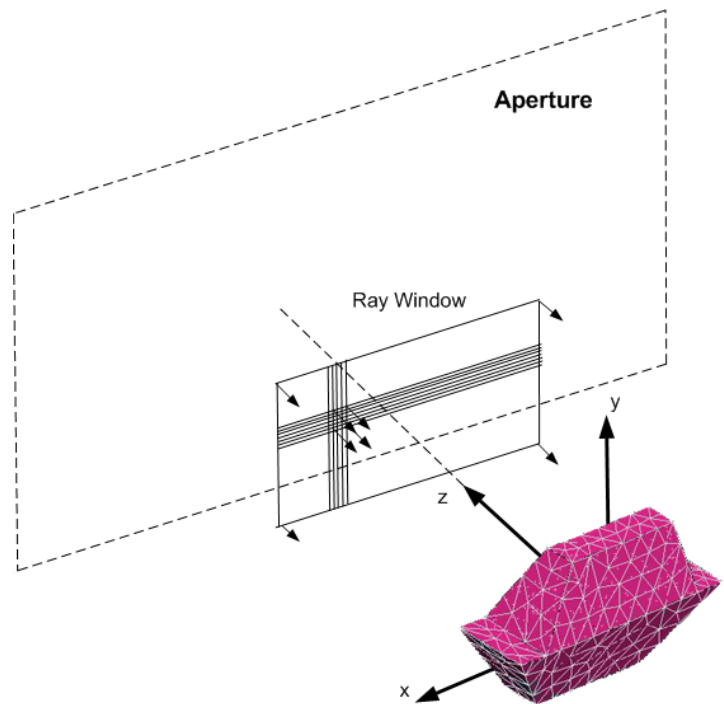


**Figure 3.1 Target and Ray Window Geometry**

In the second method, which is used for complex targets, the target is rotated.

### ***3.1 Target Modeling***

By using a superposition of simple primitive objects like prisms, spheres or cylinders, complex targets can be modeled. However, such models may suffer from precision. Surface patch representations will yield accurate target models. Triangular patches are very flexible for modeling targets effectively. However, if our geometric model has a large number of patches, the ray-triangle intersection algorithm will be the main contributor to runtime. By using brute force search techniques it is not possible to solve high frequency problems in reasonable times. In our examples, we construct geometries by using large triangular patches shown in Figure 3.3. The geometries are constructed in a Computer Aided Design (CAD)



simulated; first a tank model which is modeled by 132 triangular patches, second a simple ship model constructed from 28 triangular patches and last a stealth aircraft design constructed from 20 triangular patches, which is more like an F-117 aircraft.

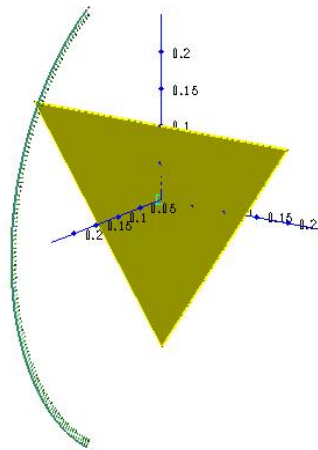


**Figure 3.3 Simulation setup for monostatic RCS of PEC triangular patch**

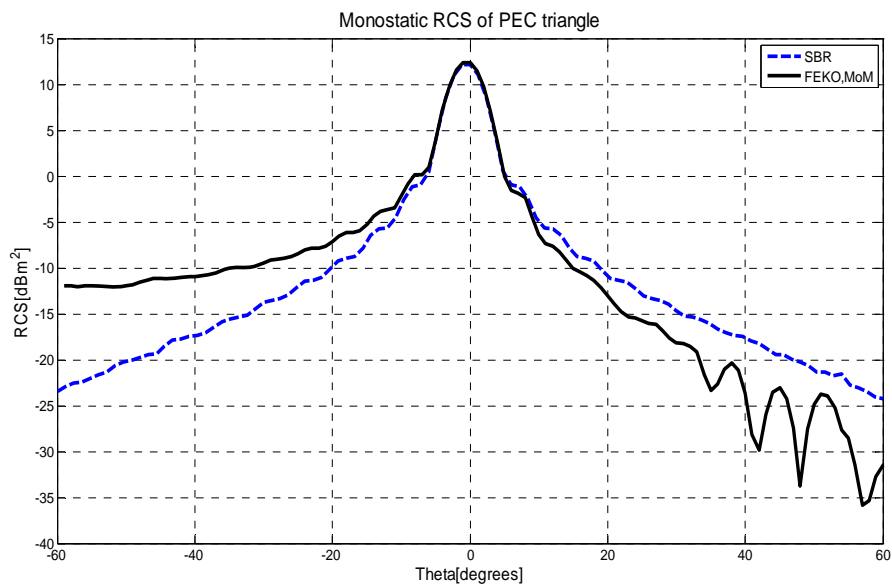


**Figure 3.4 Comparison of MoM and SBR results for  $\theta\theta$  polarized monostatic RCS of PEC triangle**

### 3.2 Target Rotation

For the visualization of RCS variation, we obtain plots of RCS versus aspect angles. Aspect angle is the orientation of target relative to the source position which is a ray window. In order to calculate the RCS as a function of aspect angle, the target is rotated. In order to rotate the target in three dimensions, three basic rotation matrices are used;

$$R_x(\alpha) = \begin{bmatrix} 1 & 0 & 0 \\ 0 & \cos(\alpha) & -\sin(\alpha) \\ 0 & \sin(\alpha) & \cos(\alpha) \end{bmatrix} \quad (3.1)$$

$$R_y(\alpha) = \begin{bmatrix} \cos(\alpha) & 0 & \sin(\alpha) \\ 0 & 1 & 0 \\ -\sin(\alpha) & 0 & \cos(\alpha) \end{bmatrix} \quad (3.2)$$

$$R_z(\alpha) = \begin{bmatrix} \cos(\alpha) & -\sin(\alpha) & 0 \\ \sin(\alpha) & \cos(\alpha) & 0 \\ 0 & 0 & 1 \end{bmatrix} \quad (3.3)$$

Each of these matrices rotates a target in counterclockwise direction around a fixed coordinate axis, by an angle of  $\alpha$ . Rotation direction is determined by the right-hand rules. Other rotation matrices are derived from these three basic matrices.

In our simulations, for rotating a target that is in STL mesh format, all vertices of triangular patches are rotated about the orthogonal axes of the global coordinate system. Simple rotation geometry is illustrated in Figure 3.5.

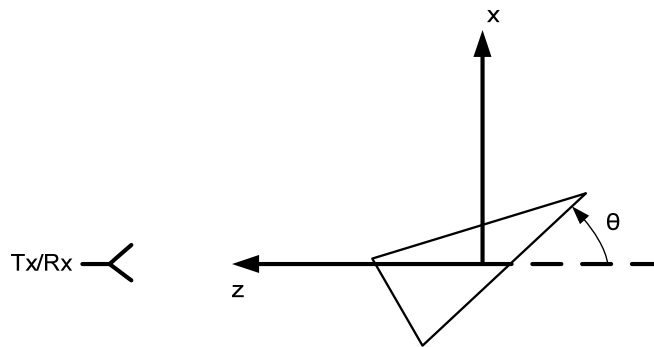


**Figure 3.5 Fixed rotation around Y axis**

### ***3.3 Numerical Results***

The first simulation is conducted on a simple tank model which has a length of 1 m and a height of 0.5 m. Monostatic RCS values are calculated at angles from  $\theta = 0^\circ$  to  $\theta = 180^\circ$  at 6GHz. The results obtained from SBR MATLAB code are compared with those obtained from the FEKO software. In these simulations, two computers are used;

Computer 1; Intel (R) Core 2 Duo CPU, E4500@2.20GHz

**3.25GB RAM**

Computer 2; (Dual) AMD Opteron™ Processor 248

**14.926 GB RAM**

The tank is modeled in CADFEKO, which is the modeling tool of FEKO software, and exported in STL mesh format. The model consists of 132 triangular patches.

- Monostatic RCS of tank model
- Polarization=vertical
- Frequency=6GHz
- Maximum dimension=1m

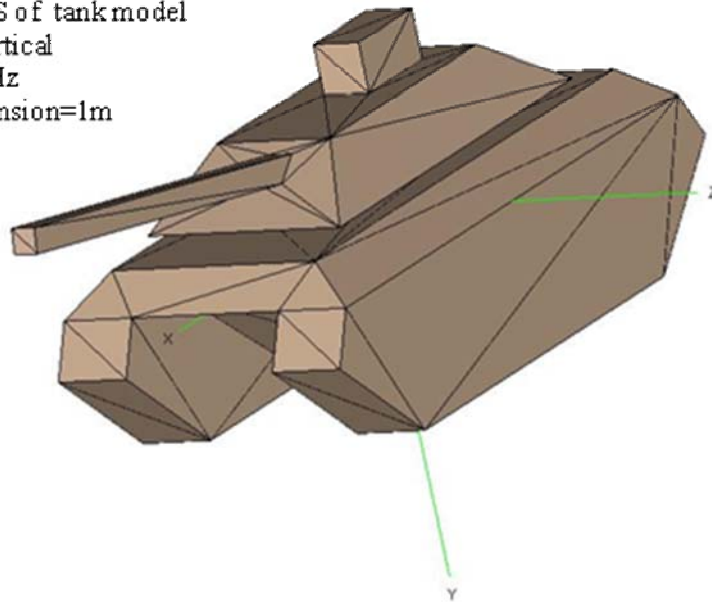
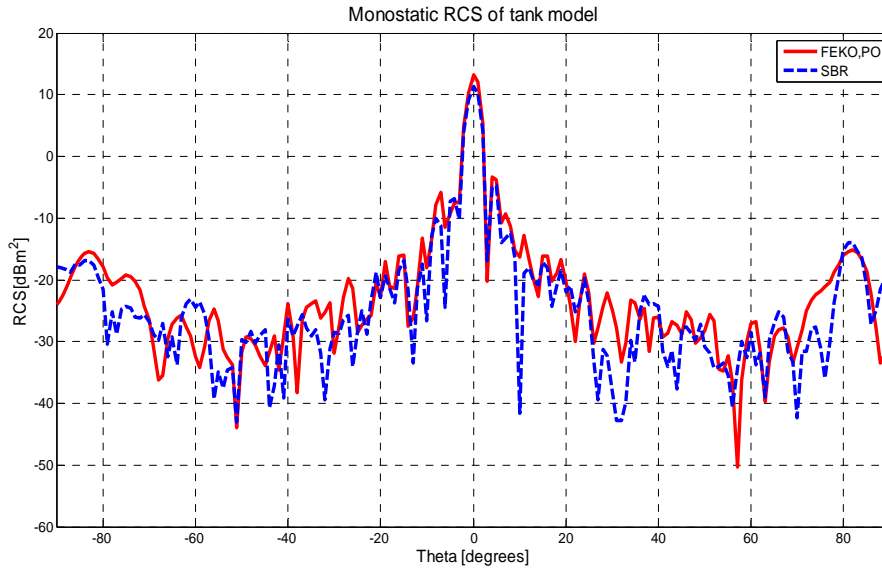


Figure 3.6 Tank model constructed from 132 triangular patches

Table 3-1 Computation times for tank model simulation

	Time/Sample Seconds	Sample	Total Time Hours	RAM MB	Computer
SBR, MATLAB	1181	181	59.4	-----	1
PO, FEKO	0.19	181	0.01	13	1



**Figure 3.7 Comparison of PO and SBR results for  $\theta\theta$  polarized monostatic RCS of PEC tank model**

The results of FEKO (PO) and MATLAB (SBR) match closely as shown in Figure 3.7. Although the model contains only a moderate number of patches, the runtime is very long due to the lack of a fast ray-triangle intersection algorithm. With brute-force ray-triangle intersection test, it takes 20 minutes to calculate the monostatic for a single aspect angle.

The second example is conducted on a simple ship model with length 1 m and height 0.5 m. Monostatic RCS values are calculated at angles from  $\theta = 0^\circ$  to  $\theta = 180^\circ$  at 6GHz. The ship is modeled in CADFEKO, modeling tool of FEKO software, and exported in STL mesh format. The model consists of 28 triangular patches. In this example, the solution is obtained by using a planar exit aperture. Although we have mentioned that the conformal aperture approach yields optimum results, this example shows that the planar exit aperture choice can give good results for targets whose scattering characteristics are dominated with specular regions.

- Monostatic RCS of ship model
- Polarization=vertical
- Frequency=6GHz
- Maximum dimension=1m

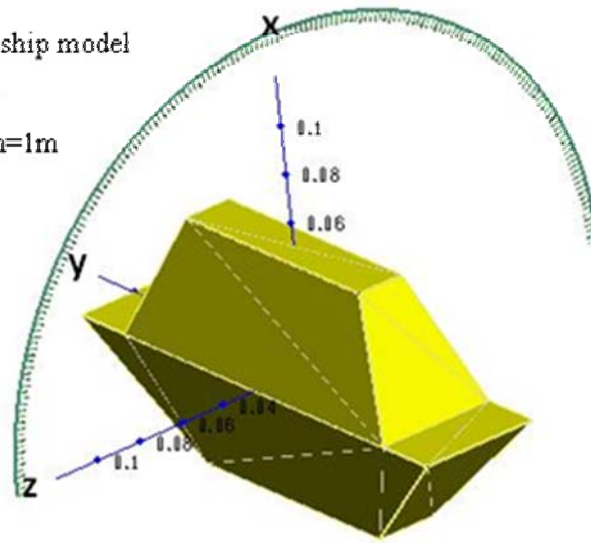
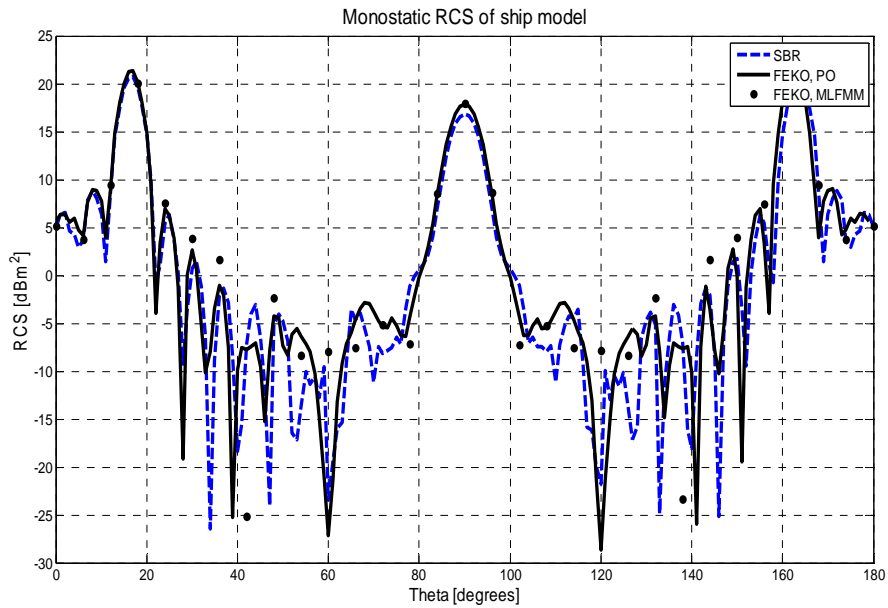


Figure 3.8 Monostatic RCS of ship model

Table 3-2 Computation times for ship model simulation

	Time/Sample Seconds	Sample	Total Time Hours	RAM MB	Computer
SBR, Matlab	551	151	23.2	-----	1
PO, FEKO	0.25	181	0.012	13	1
MLFMM, FEKO	2880	31	24.9	875	2



**Figure 3.9 Comparison of PO, MLFMM and SBR results for  $\theta\theta$  polarized monostatic RCS of PEC ship model**

The results obtained from FEKO (PO and MLFMM) and SBR agree well in specular regions. Due to the fact that specular scattering is dominant in this model the results match closely with those obtained by FEKO (MLFMM) in the wide spectrum from  $\theta = 0^\circ$  to  $\theta = 180^\circ$ .

The third simulation is conducted on a stealth aircraft design [11], which is 1 m long and has a 1 m wing span. The monostatic RCS values are calculated at angles from  $\theta = 30^\circ$  to  $\theta = 150^\circ$  at 6GHz. The results obtained from the SBR MATLAB code are compared with the results of the FEKO software.

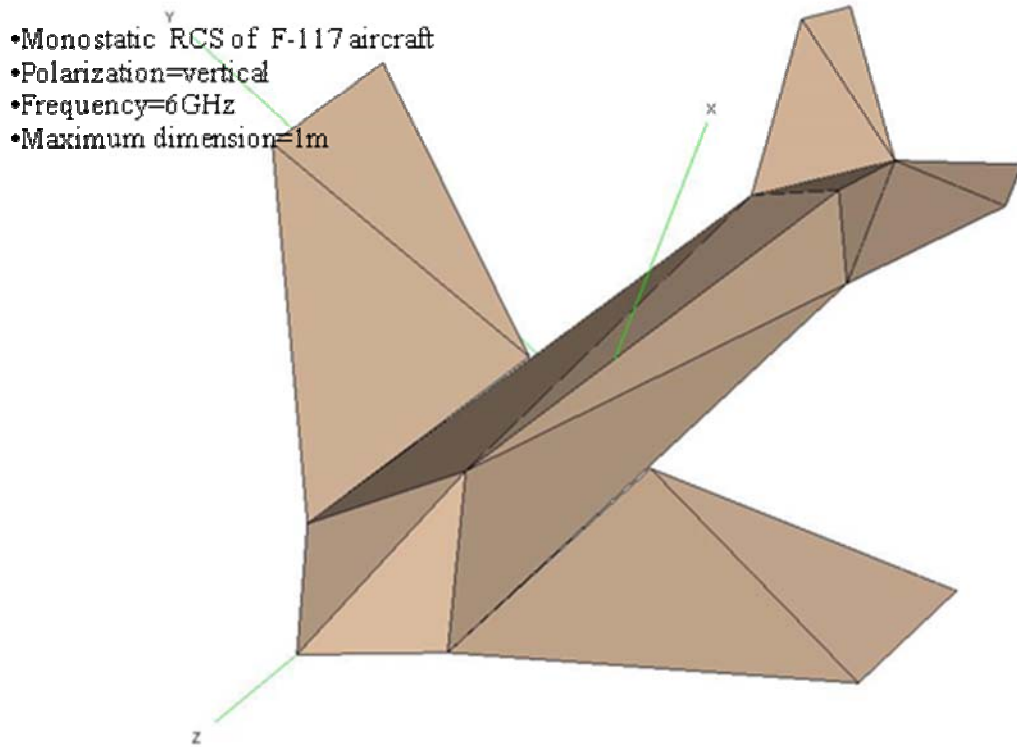


**Figure 3.10 F-117 model**

**Table 3-3 Computation times for F-117 model simulation**

	Time/Sample Seconds	Sample	Total Time Hours	RAM MB	Computer
SBR, MATLAB	276	121	9.27	-----	1
PO, FEKO	0.78	121	0.026	20	1
MLFMM, FEKO	2484	121	83.49	875	2

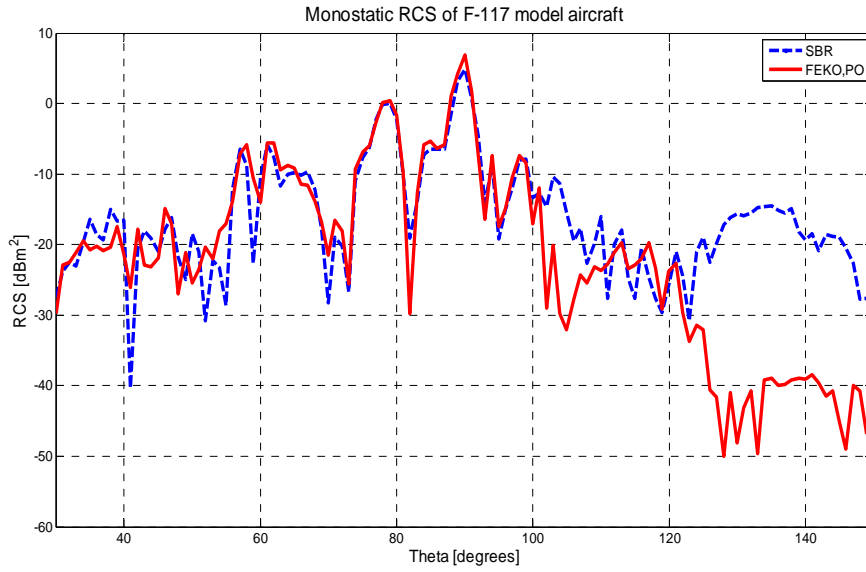


**Figure 3.11 Comparison of PO and SBR results for  $\theta\theta$  polarized monostatic RCS of PEC F-117 model**

The results of PO and SBR agreed for the angles between  $0^0 < \theta < 120^0$  as shown in Figure 3.11. For the angles  $120^0 < \theta < 150^0$ , the results are not consistent.

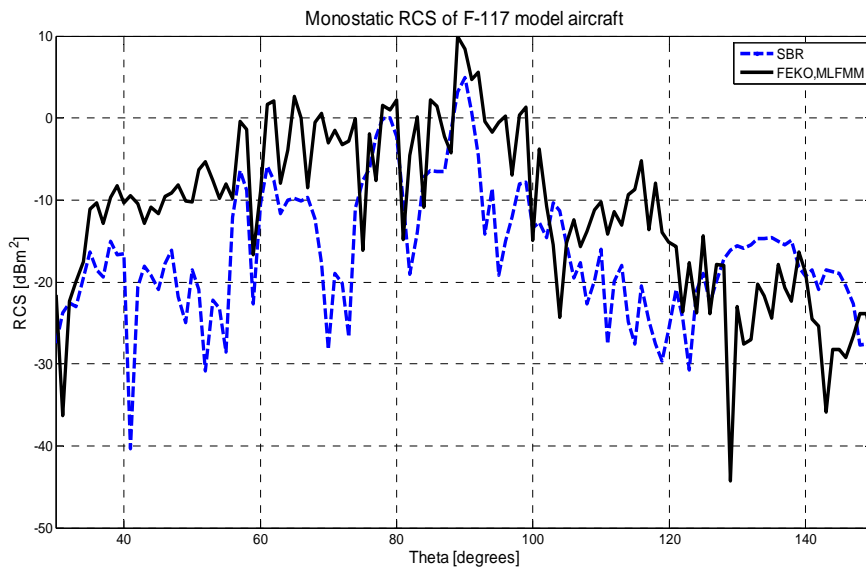


**Figure 3.12 Comparison of MoM and SBR results for  $\theta\theta$  polarized monostatic RCS of PEC F-117 model**

When the results are compared with those obtained by the MLFMM code, it is clear that the results do not match closely. The main reason of this inconsistency is the diffraction weighted structure of the geometry. Since the geometry is a stealth aircraft, specular reflections are avoided for all angles. Also, the SBR code does not include a multiple scattering capability for complex targets. This is the second reason for the inconsistency between the results of SBR and MLFMM.

## CHAPTER 4

### CONCLUSIONS

#### *4.1 Summary of the Thesis*

A MATLAB code based on SBR is implemented to compute the RCS of complex targets. Results are compared with both full-wave and high frequency methods of FEKO software. Basically, SBR is a high frequency method that combines the advantages of Geometric Optics (GO) and Physical Optics (PO) approaches.

In SBR, rays that simulate the incident plane wave are shot towards the target, bounce back and forth between the facets modeling the PEC object surface and finally are captured in an exit aperture. The phase and amplitude of the electrical field is propagated along the rays with the GO rules. In an exit aperture outgoing rays are captured and the field can be determined. With the PO approximation a current sheet is determined in the aperture. Integration in this aperture is not easy to carry out. Instead of this, a small ray tube is shot towards the geometry and the scattered field is computed by taking into account its size and shape. With a sufficient number of ray tubes that models the incident field shot into the geometry, the RCS is calculated.

SBR was implemented for the first time to solve cavity problems, in which the exit aperture is the mouth of the cavity, which guarantees that all the outgoing rays are captured there. In this thesis, the method is implemented for open

scatterers where the exit aperture selection is critical. A new exit aperture configuration named as “conformal aperture” is proposed and the results of this configuration are compared with those obtained via the common aperture selections. With this aperture configuration, the results matched the PO results.

The results obtained from the MATLAB code match closely with PO and MoM results near specular regions. Out of the specular regions, the results do not match due to the fact that diffraction effects are not modeled in the code. Basically, SBR is a multiple scattering algorithm. This capability of the code is investigated and verified. Also, it is a ray tracing approach which handles the shadowing problem easily.

Some complex target models are generated in CADFEKO tool and imported to SBR code in STL mesh format. For the ray-triangle intersection test, brute-force methods are used which turned out to be the main reason for the excessively long run-times. This difficulty led us to consider targets modeled with a moderate number of patches.

The code is developed in MATLAB 2007b version. There is no need a special MATLAB toolbox to implement this algorithm.

## ***4.2 Advantages and Disadvantages of SBR***

RCS prediction tools are generally used to design stealth structures. In stealth designs usually specular reflections, that contribute a lot to the RCS, are tried to be avoided. Therefore, for such applications it becomes crucial to predict multiple scattering and/or diffraction effects. SBR is a code that handles multiple scattering up to any arbitrary order. With the help of diffraction codes like Physical Theory of Diffraction (PTD) or Geometric Theory of Diffraction (GTD), this algorithm can be useful for simulations that are utilized in stealth design. Also, SBR can

handle shadowing problem automatically with the help of its ray tracing capability.

Since SBR is a ray tracing based approach, it is not efficient unless a fast ray-triangle intersection algorithm is used. With brute force methods in ray-triangle intersection, it is not feasible to handle realistic problems modeled by a large number of facets.

### ***4.3 Future Work***

In this work, a computational electromagnetics code is created by using the SBR algorithm in MATLAB. It is stated that for open scatterers the exit aperture selection is critical. A conformal exit aperture algorithm is developed and applied over complex targets. The code is tested for its multiple scattering capabilities. For future work, the code can be modified and expanded to handle dielectric structures and coatings. Also, with brute-force ray-triangle intersection test, the code is not efficient with regard to runtime. With a fast ray-triangle intersection algorithm, like mailbox or kd-tree, the code can be efficiently used for more realistic targets.

The SBR algorithm cannot handle diffraction effects. So, by including a routine that handles diffraction effects (i.e. a code based on Physical Theory of Diffraction (PTD) or Geometric Theory of Diffraction (GTD)), the code can be used in stealth design applications. Another application may be the generation of Inverse Synthetic Aperture Radar (ISAR) images with the help of SBR code.

A computational electromagnetic tool that only calculates the RCS of realistic targets is not sufficient to achieve stealth design. By visualization tools like ISAR imaging or range profiling, scattering centers on a target can be detected. It is possible to create the ISAR image of a target from monostatic or bistatic RCS data of the SBR code. This will be the post processing stage of the SBR code and

may help us to find and/or annihilate scattering centers of objects in stealth applications.

## REFERENCES

- [1] Chou R., Ling H., Lee S.W., *Reduction of the Radar Cross Section of Arbitrarily Shaped Cavity Structures*, Technical Report, University of Illinois August 1987, No. 87-6.
- [2] Ling H., Chou R., Lee S.W., *Shooting and Bouncing Rays: Calculating the RCS of an Arbitrarily Shaped Cavity*, IEEE Transactions of Antennas and Propagation, Vol. 37 No.2, February 1989, pp. 194-205.
- [3] Baldauf J., Lee S.W., Lin L., Jeng S., Scarborough S., Yu C.L., *High Frequency Scattering from Trihedral Corner Reflectors and Other Benchmark Targets: SBR Versus Experiment*, IEEE Transactions of Antennas and Propagation, Vol. 39 No. 9, September 1991, pp. 1345-1351.
- [4] Galloway E.R., Welsh T.D., *Extension to the Shooting Bouncing Ray Algorithm for Scattering from Diffusive and Grating Structures*, International Radar Symposium, India, 2005.
- [5] Comprehensive Electromagnetic Solutions FEKO, <http://www.feko.info/>, last visited on August 2009.
- [6] Lee S.W., Chou R., Ling H., *Ray-Tube Integration in Shooting and Bouncing Ray Method*, Microwave and Optical Technology Letters, Vol.1 No.8, October 1988, pp. 286-289.
- [7] Lee S.W., Mittra R., *Fourier Transform of a Polygon Shape Function and Its Application in Electromagnetics*, IEEE Transactions on Antennas and Propagation, Vol. AP-31, No. 1, January 1993, pp. 99-103.
- [8] Albayrak N.A., *RCS Computations with PO/PTD for Conducting and Impedance Objects Modeled as large Flat Plates*, M.Sc. Thesis, Bilkent University, Ankara, July 2005.

- [9] Marschner S., *CS465 Notes: Simple Ray-Triangle Intersection*, Course Notes, Cornell University, October 2003
- [10] Chu F., Huang C., *On the Calculation of the Fourier Transform of a Polygonal Shape Function*, Journal of Physics A: Mathematical and General, Vol. 22 No. 14, Department of Electrical Engineering of Tatung Institute of Technology , April 1989, pp. 671-672.
- [11] RCS Calculations Using the Physical Optics Codes, <http://aircraftdesign.nuaa.edu.cn/lo/software/pocodes.pdf>, last visited on August 2009.